Tectonophysics 800 (2021) 228708

Contents lists available at ScienceDirect

Tectonophysics

journal homepage: www.elsevier.com/locate/tecto

Structural and chemical resetting processes in white mica and their effect on K-Ar data during low temperature metamorphism

Ismay Vénice Akker [a,*], Alfons Berger [a], Horst Zwingmann [b], Andrew Todd [c], Christoph E. Schrank [d], Michael W.M. Jones [e], Cameron M. Kewish [f,g], Timothy C. Schmid [a], Marco Herwegh [a]

[a] Institute of Geological Sciences, University of Bern, Bern, Switzerland
[b] Division of Earth and Planetary Sciences, Graduate School of Science Kyoto University, Kyoto, Japan
[c] Commonwealth Scientific and Industrial Research Organisation (CSIRO), Earth Science and Resource Engineering, Bentley, Australia
[d] School of Earth and Atmospheric Sciences, Queensland University of Technology, Queensland 4000, Australia
[e] Central Analytical Research Facility, Institute of Future Environments, Queensland University of Technology, Queensland 4000, Australia
[f] Department of Chemistry and Physics, La Trobe Institute for Molecular Science, La Trobe University, Victoria 3086, Australia
[g] Australian Nuclear Science and Technology Organisation, Australian Synchrotron, Victoria 3168, Australia

ARTICLE INFO

Keywords:
Microstructure
Phyllosilicates
K-Ar
Recrystallization
Metamorphism

ABSTRACT

White mica has been widely used to date microstructures and tectonic events in faults, shear-zones and folds because of its suitability for radiogenic dating. However, complex (i) microstructural evolution, (ii) individual chemical evolution of the K-bearing phases, (iii) mixing of 'detrital grains' with newly formed and/or recrystallized or chemically reset grains as well as (iv) volume diffusion may result in apparent K-Ar ages. Here, specimens from a prograde sediment sequence of the exhumed fossil European Alpine accretionary wedge were used to investigate resetting processes of white mica by the type and intensity of deformation as well as peak metamorphic conditions. We combine the K-Ar system with mass and mineral quantities from grain size fractions to calculate the amount of recrystallized white mica in each grain size fraction along the metamorphic gradient. Increasing recrystallization with increasing metamorphic grade is related to thermally activated pressure solution and dissolution-precipitation creep, as seen by the formation of a spaced cleavage of recrystallized phyllosilicates documented through Synchrotron X-ray Fluorescence Microscopy and Scanning Electron Microscope imaging techniques. Increasing recrystallization by dissolution-precipitation processes induces chemical resetting of the isotopic system, resulting in a prograde decrease of apparent K-Ar ages. We demonstrate that Ar volume diffusion does not play a significant role for the low-temperature samples, promoting recrystallization as the important physico-chemical process for age resetting. However, white mica chemistry reveals that no simple relation between isotopic resetting and grain size exists along the prograde path. Reliable age information can therefore only be obtained in the case of (nearly) complete resetting, which accounts only for the smallest grain size fraction at the highest metamorphic temperature. These findings could shed new light on accurate dating of mica-rich fault rocks, where the time constraints depend not only on the temperature, but also on the amount and type of deformation.

1. Introduction

In subduction zones, the initially porous and fluid-saturated marine sediments dehydrate while being incorporated into the accretionary wedge and subducted under the upper plate (e.g., Dielforder et al. (2015) and references therein). With increasing finite strain, the interconnectivity of phyllosilicates in layers and networks forms weak zones and results in an anisotropic rock texture along which deformation can easily localize (White and Knipe, 1978). This weakening enables slip along brittle faults, in the case of upper-crustal or rapidly deformed mid-

* Corresponding author.
E-mail addresses: ismay.akker@geo.unibe.ch (I.V. Akker), alfons.berger@geo.unibe.ch (A. Berger), zwingmann.horst.4a@kyoto-u.ac.jp (H. Zwingmann), andrew.todd@csiro.au (A. Todd), christoph.schrank@qut.edu.au (C.E. Schrank), mw.jones@qut.edu.au (M.W.M. Jones), cameronk@ansto.gov.au (C.M. Kewish), timothy.schmid@geo.unibe.ch (T.C. Schmid), marco.herwegh@geo.unibe.ch (M. Herwegh).

https://doi.org/10.1016/j.tecto.2020.228708
Received 19 August 2020; Received in revised form 8 December 2020; Accepted 15 December 2020
Available online 4 January 2021

crustal phyllosilicate-rich rocks (e.g. Torgersen and Viola (2014)) and somewhat wider localized shear in ductile shear zones (Passchier and Trouw, 2005). Among the suite of phyllosilicate minerals, white mica is of particular interest because of its suitability for radiogenic dating of crustal-scale deformation (e.g. (Torgersen et al., 2015a)). Moreover, white mica is stable under a wide range of metamorphic conditions, and it defines deformation fabrics, which are especially well pronounced in slates (Dunlap et al., 1991).

The isotopic K-Ar and ^{40}Ar-^{39}Ar systems of white mica have been widely used to date microstructures and tectonic events in brittle faults, shear-zones and folds (e.g. Fitz-Diaz and van der Pluijm (2013); (Torgersen et al., 2015a); van der Pluijm et al. (2006); Viola et al. (2013); Wang et al. (2016)). However, the Ar system is less well understood during diagenesis of low to very-low grade metamorphic slates due to complex microstructures and the individual chemical evolution of the K-bearing phases. In studies using multigrain separates, radiometric ages commonly reflect several mineral populations (Berger et al., 2017; Villa et al., 2014). The term 'recrystallization' as used in this paper includes static and dynamic recrystallization or neocrystallization (formation of new grains), by which re-equilibration of the initial geochemical composition results in (partial) 'resetting' of the chemical and isotopic composition (e.g., Clauer et al. (1997)). Other microphysical processes responsible for the final composition of micas on the retrograde path include: (1) (re)-precipitation of newly fine-grained white mica (Dempster, 1992), (2) dissolution-(re)-precipitation (Airaghi et al., 2017; Putnis, 2002) and (3) remnant grains. Berger et al. (2017) investigated these processes in mica along the retrograde path (Aar massif, Central Alps, CH). Until now, it is not clear what the contribution of each single process to resetting is and how these are expressed on the prograde path in phyllosilicate-rich systems, as for example in sediments of active accretionary wedges.

The K-Ar system of white mica is well suited to study the effect of recrystallization on the resetting process (Clauer, 2013). Using the K-Ar system, Pevear (1999) developed a method to quantify the detrital and diagenetic endmember ages for shales. Quantification of the different resetting processes (e.g. Airaghi et al. (2018); McDonald et al. (2016); Mulch and Cosca (2004)) is the missing link between multigrain isotope data and local in-situ microstructures and petrology. Therefore, we combine quantitative mineral separation with microstructures and isotope data to potentially link grain sizes, microstructures and isotope data and identify the correlation with the mineral chemistry of the selected minerals. Knowledge on such resetting processes is of great importance because dehydration is thought to represent one of the important processes in resetting the Ar system (Bosse and Villa, 2019; Villa and Hanchar, 2013). Independent evidence for high fluid contents is the intensity of veining (Akker, 2020: Dielforder et al., 2015), which itself also plays an important role in triggering seismic activity in such highly active geodynamic domains (e.g. Dielforder et al. (2016); Dielforder et al. (2015); Moore and Saffer (2001); Zwingmann et al. (2019)).

Here, we investigate the behaviour of white mica in sequence of deformation and temperature in metasediments on the prograde path, specifically during the evolution of pervasive cleavage formation in slates. We use the Flysch units of the Glarus Alps (Central Switzerland) as an exhumed example of a fossil accretionary wedge, which preserve a metamorphic peak temperature gradient ranging from 200 to 330 °C (Fig. 1). A major advantage of the chosen study area is the preservation of temperature and deformation gradients, whereas the units show sedimentary differences on a regional scale. However, for this study we only select slate-rich intervals with similar mineral assemblages in order to minimise the effect of primary variations in the sedimentary evolution.

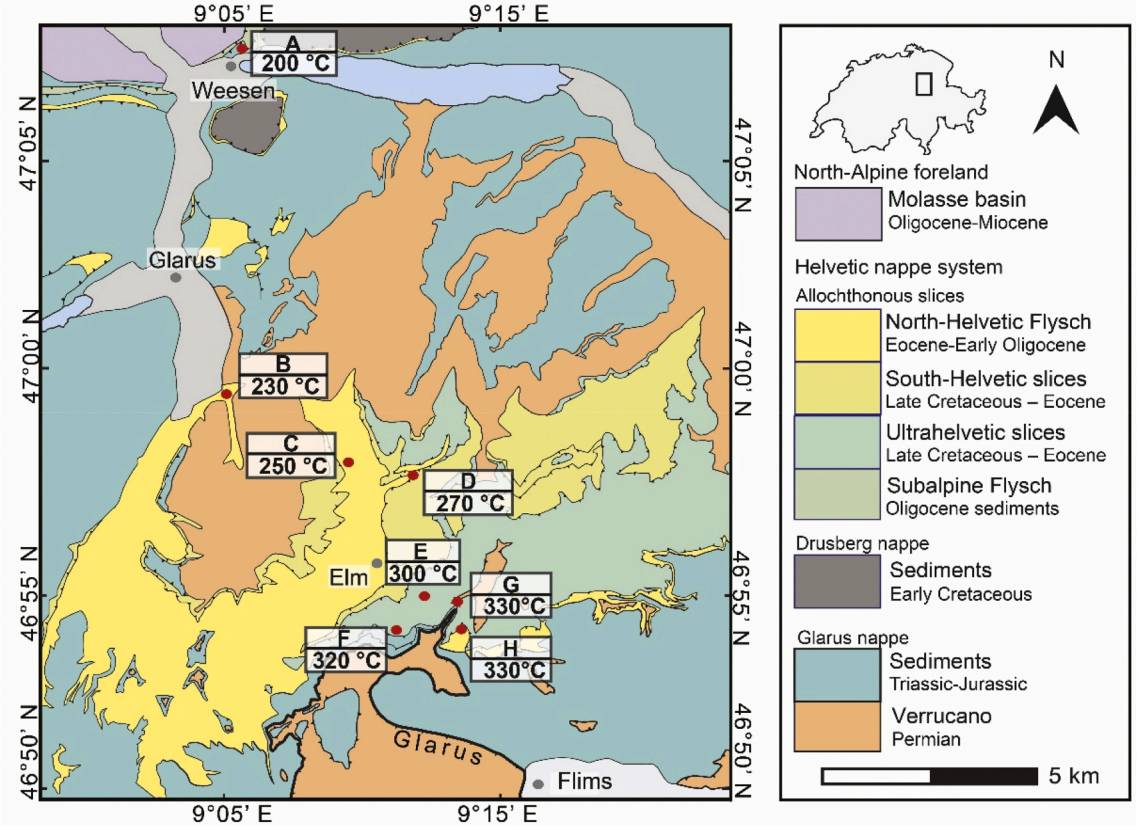

Fig. 1. Geological map with sample locations. Map after Dielforder et al. (2016). Peak metamorphic temperatures from Ebert et al. (2007), Rahn et al. (1995) and Lahfid et al. (2010). Light blue area is lake Walensee and the light grey areas are river valleys.

2. Geological background and samples

The European Alps were formed due to collision between the European and Adriatic plate. In the Mesozoic, both the European and Adriatic plate were dominated by carbonate sediments at their margins, which were deposited on prior rifted continental crust (e.g., Lemoine and Trümpy (1987)). The former southern European margin is now preserved in the Helvetic domain (Pfiffner et al., 2011). With the inversion from extension to compression tectonics, the depositional environment changed, leading to orogenic Flysch deposits in underfilled orogen-parallel ocean basins (Sinclair, 1997). These are typically mass flow processes manifested as turbidites and associated marine sediments.

The study area is located in central Switzerland between the village of Weesen in the north and the locality Flims in the south (Fig. 1). The preserved sediments represent the final stages of Flysch sedimentation when the Ultra-, South-, and North-Helvetic realm (Fig. 2) became progressively incorporated into the accretionary prism of the emerging Alps. This ended in continent-continent collision with a change from Flysch to Molasse deposition (Sinclair, 1997). For this study, eight samples (about 300-500 g each) were taken from slate-rich lithologies from these Flysch units along an increasing metamorphic gradient (Fig. 1 and Table A.1). Data from calcite-dolomite thermometry (Ebert et al., 2007), Raman spectroscopy on carbonaceous material (Lahfid et al., 2010) and fluid inclusion data (Rahn et al., 1995) indicate that peak metamorphic temperatures increase throughout the different Flysch units from north to south from 200 °C to 330 °C.

The Ultrahelvetic Sardona unit comprises a continuous series of Cenomaninan-Campanian (97-74 Ma) Globotruncana limestone and marl as well as Maastrichtian-Bartonian Flysch deposits (Lihou and Allen (1996); Fig. 2). The Globotruncana limestone and marl are interpreted as hemipelagic sediments deposited in a starved deep marine environment (Lihou and Allen, 1996) while still being part of the European passive margin. In the Maastrichtian (74-65 Ma), foreland basin sedimentation commenced with the deposition of siliciclastic Flysch. The resulting Infraquartzite Flysch unit, mostly consisting of calcareous turbidites, shows that sediment input from the orogenic wedge was restricted and input mostly originated from a southerly sediment source, which could be the North Prättigau Swell, identified as a structural high (Rüefli, 1959). In the Paleocene to early Eocene (65-50 Ma), there was a transition from calcareous to siliceous turbidite sedimentation related to a relative sea level fall, which led to erosion of the shelf. These deposits are represented by the Sardona quartzite formation (Lihou and Allen, 1996) and did not only have sediment input from the southerly located North Prättigau Swell but also from the uplifted northerly located South Helvetic Swell (Rüefli, 1959). In the middle Eocene (50-40 Ma), the entire shelf was flooded due to a transgression. In the Sardona basin, the youngest Flysch unit, the Supraquartzitic Flysch, was deposited and records the transition back to calcareous turbidite sedimentation (Lihou and Allen, 1996). Along with the final stages of accretion, the tectonic Austroalpine and Penninic nappes were piled upon the Flysch units when the accretionary wedge formed the tectonically active plate boundary. With the subsequent onset of continent-continent collision, a large-scale out-of-sequence thrust, the Glarus thrust, decapitated the entire prism geometry by bringing Helvetic nappes on the formerly imbricated Flysch units (e.g. Schmid (1975)), leading to peak metamorphic overprint of the Flysch units (Ebert et al., 2007; Herwegh et al., 2008; Lahfid et al., 2010).

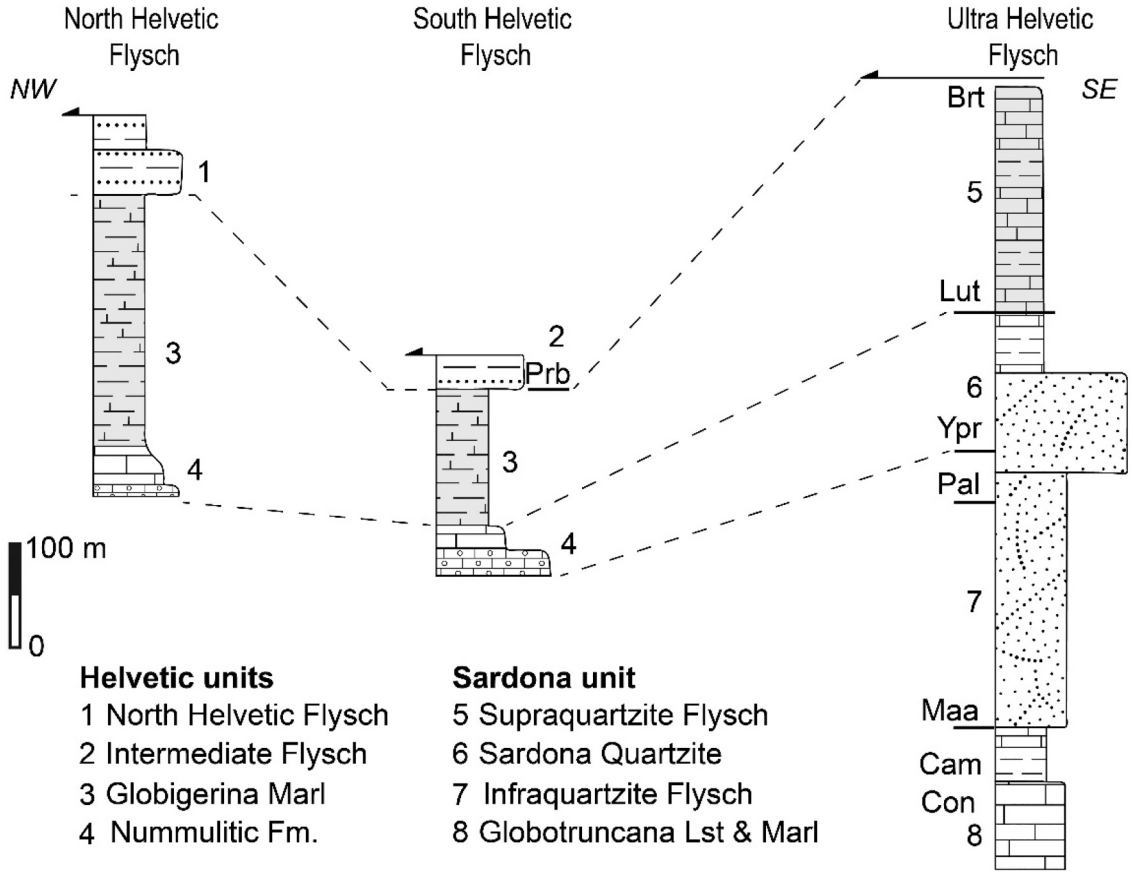

Fig. 2. Stratigraphy of the Flysch units from Lihou and Allen (1996). The stippled lines connect iso-sedimentation-age intervals demonstrating diachronous formation of some units. Con: Coniacian, Cam: Campanian, Maa: Maastrichtian, Pal: Paleocene, Ypr: Ypresian, Lut: Lutetian, Brt: Bartonian, Prb: Priabonian.

3. Methodology

3.1. Microstructural imaging

Thin sections were cut from rocks and studied with a petrographic microscope (Zeiss Axioplan) to confirm mineralogy and microstructure and to select areas of interest for scanning electron microscopy (SEM) and electron microprobe analysis (EPMA; see below). We used a Zeiss EVO 50 SEM with backscatter and secondary-electron detectors at the Institute of Geological Sciences, University of Bern, to obtain high-resolution microstructure images of the selected areas of interest.

3.2. Grain size separation and estimation of mass fractions

For grain size separation of the slate rocks, a combination of high-voltage disintegration Selfrag™ and a gravity-settling technique, based on Stokes law (Fig. 3, stage 1 to 3), was used at the Institute of Geological Sciences, University of Bern. The high-voltage disintegration method has been proven to be a reliable disintegration technique in claystones for the use of isotope geochronology (Zwingmann et al., 2017). Starting volumes for Selfrag™ were about 314-543 grams of whole rock. The rocks were disintegrated with 15 pulses with a 25 mm electrode gap, followed by 200 to 400 pulses with a 20 mm electrode gap. Operating conditions of the Selfrag™ were 3 Hz and 150 kV. This method uses significant amounts of water, which was collected and eventually reduced using a centrifuge to minimise the loss of any sample material. From all collected disintegrated sample material, a whole-rock sample was separated. All material was subsequently sieved (wet with a one-way sieve) to 64 µm, after which water was again reduced using a centrifuge, and all sample material was dried at 38 °C.

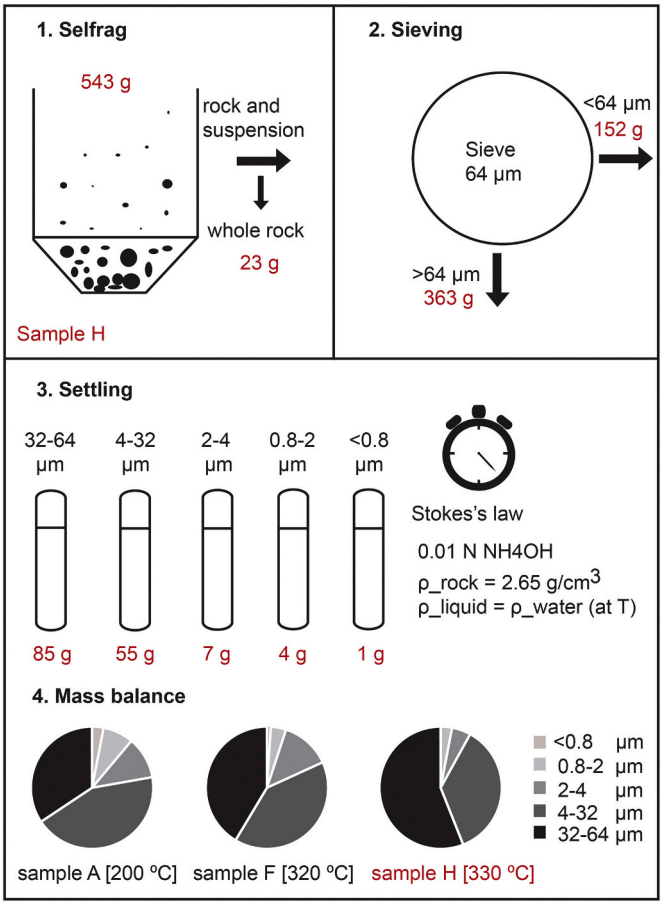

Fig. 3. Methodology for grain size separation and mass data of fractions. Three main steps in grain size separation: Selfrag™ electric pulse disaggregation (1), wet sieving (2) and settling (3). The weight from sample H is indicated from the start to the end of the process (numbers in red). The loss from the Selfrag™ and sieving process (1 and 2) is 0.7% and from the settling process (3) is 0.6% from the total weight of the rock at the start of the process (Supplementary Material).

The gravity settling was performed in Atterberg cylinders (20 cm high). The cylinders were each filled with 15-20 grams of sample material (<64 µm) and ionised for about 4 minutes to prevent the formation of grain aggregates before a NH_4OH 0.01N solution was added. Settling times were calculated using SediCalc software (from Stefan Krumm, software published in 2006). The following grain size fractions were separated from the whole rock: <0.8 µm, 0.8-2 µm, 2-4 µm, 4-32 µm, 32-64 µm. In the case of the sample with the highest metamorphic grade, only 1 g sample material was obtained for the grain size fraction <0.8 µm, possibly due to thermal grain growth processes during metamorphism (see below). Owing to the sample nature, it was not feasible to separate sufficient fine fraction material of <0.1 µm. The accurate weight of the dry whole rock at the start was compared with the sum of the obtained grain size fractions after the grain size separation process (Fig. 3, stage 4 and Supplementary Material). These weights are needed in a next step for 'mass proportion calculations'.

3.3. Mineral chemistry

3.3.1. X-ray Powder Diffraction (XRD)

All X-ray powder diffraction (XRD) measurements were carried out and analysed at the Institute of Geological Sciences, University of Bern. Measurements were performed on non-oriented samples of the separated grain size fractions. Corundum was used as internal standard, in order to perform a quantitative analysis. Corundum was milled in fractions of 5 g Al_2O_3 and 10 ml ethanol for 10 minutes on half speed in a "McCrone mill" (Retsch), before mixing with the sample.

The measurements of the non-oriented samples were performed with a PANalytical CubiX^3 diffractometer, equipped with a Cu source and a secondary beam graphite monochromator. The data were collected from 5 to 75° 2Θ with a step size of 0.02° 2Θ, 1.5 s integration time per step and a fixed divergence slit of 1/4°. All quantitative phase analyses were performed with Topas-Academic (Coelho Software). The diffraction patterns were first refined using the Rietveld method, yielding quantitative information about all included phases. An overview of used phase structures for refinements can be found in Appendix B. However, due to unknown structural and chemical features, Rietveld quantification of clay minerals is problematic and may bias results of all other phases (e.g. Kemp et al. (2019)). Therefore, combined Rietveld/Pawley approaches were applied (Pawley, 1981). In this case, clay minerals are not directly accounted for in the quantification process. For the pure Rietveld refinements, admixed corundum was used to determine the amount of amorphous or undetermined material. Combined Rietveld/Pawley refinements yield the amount of amorphous/undetermined phases, including all clay minerals. The comparison of pure Rietveld and combined Rietveld/Pawley refinements allows us to observe accurate trends of all non-clay minerals, whereas the pure Rietveld refinements may give insight about changes in the clay mineral fractions. We used the Pawley approach as a quality control on the Rietveld data. We found the total amount of amorphous or undetermined minerals plus clay minerals from both refinements yield acceptable differences (Supplementary Material), and therefore only the Rietveld data are discussed in the results below.

To detect the presence of mixed-layers illite/smectite, we made additional diffractometer diagrams of oriented samples from the grain size fractions (Appendix Fig. B.1). The oriented samples on glass plates were measured: 1) in air and, 2) directly after being in an ethylene glycol atmosphere at 50 °C for 24 hours. The latter treatment induces swelling of clay minerals, which would be visualized in the obtained patterns. Measurements were performed with a Philips Analytical PW3710 diffractometer, equipped with a Cu anode from 2 to 40° 2Θ and a step size of 0.02° 2Θ, with 1 s integration time per step and a fixed divergence

slit of 1°.

The absolute phase amount per grain size fraction, or the mass proportion, was obtained from the mass data of the fraction weight (Fig. 3, step 4) and the evaluated quantity of each mineral in each fraction (Fig. 4a). We calculate the mass proportion of the grain size fractions, from the weights measured beforehand, to the whole rock weight. Secondly, we calculate how much of the measured volume phase from the XRD is present in each of these proportional grain size fractions, for each sample (Fig. 4b and Supplementary Material).

3.3.2. *Electron microprobe analysis (EPMA)*

A JEOL 8200 superprobe instrument was used at the Institute of Geological Sciences, University of Bern. We performed spot analysis to obtain chemical quantification of white mica. For standardization we used anorthite (Ca, Al), orthoclase (Si, K), albite (Na), olivine (Mg, Fe), ilmenite (Ti), Tephroite (Mn). We applied a 3 µm spot size, an acceleration voltage of 15 kV and a current of 10 nA. Due to the spot size limitation, grains smaller than 3 µm were not analysed. For white mica, oxides were recalculated to cations by the use of 12 oxygens and 2 hydrogens.

3.4. *K-Ar dating*

Conventional K-Ar dating was used instead of ^{40}Ar-^{39}Ar dating, since the latter, especially regarding fine-grained clay minerals, is affected by ^{39}Ar recoil during sample irradiation and requires non-standardized corrections (Clauer et al., 2012). K-Ar dating was carried out at the CSIRO Energy facilities in Perth, Australia, on the following grain size fractions: <0.8 µm, 0.8-2 µm, 2-4 µm, 4-32 µm and whole rock splits. K content was determined by ICP-OES (Agilent), and ~ 20 mg dry sample aliquots were dissolved with HF and HNO_3 (Heinrichs and Herrmann, 2013). The samples, once in solution, were diluted to ~ 20 ppm K for the ICP-OES analysis. The error of K determinations of all samples and K standard (MA-N) is below 2% (2 σ). Ar isotopic determinations were performed using a procedure similar to that described (Bonhomme, 1975). For Ar analysis by noble gas spectrometry, ~20 mg sample splits were loaded into clean Mo foil (Goodfellow molybdenum foil, thickness 0.0125 mm, purity 99.9%), weighed and subsequently heated to 80 °C overnight to remove moisture, and reweighted using a Mettler AT20 balance. The measured dry weight was used in the K-Ar age calculation. Samples were stored in a desiccator prior to loading into the Ar-extraction vacuum line. Once loaded, the samples were heated under vacuum at 80 °C for several hours to reduce the amount of atmospheric

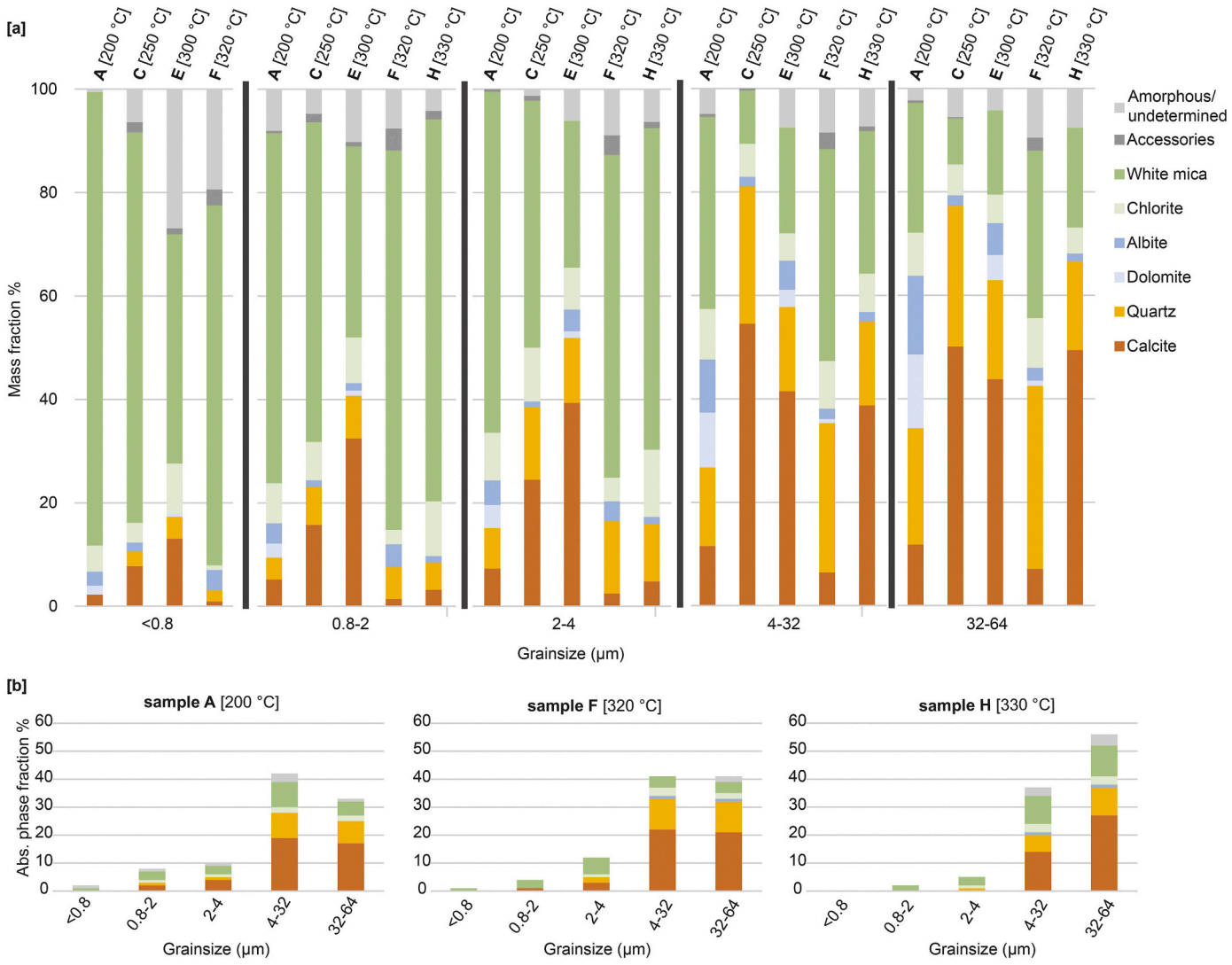

Fig. 4. Mineralogical quantification (XRD data) combined with mass proportion calculations of grain size separates. a) The XRD data show that the amount of clasts increases and the total amount of phyllosilicates decreases with increasing grain size. b) Mass proportion results yield the absolute amount of different phases (on y-axis in %) in each grain size fraction (on x-axis in µm) for three samples along the metamorphic gradient.

Ar adsorbed onto the mineral surfaces during sample handling. Ar was extracted from the test portions by fusing them in a furnace attached to the vacuum line, containing an on-line ^{38}Ar spike pipette. The isotopic composition of the spiked Ar was measured with an on-line VG3600 mass spectrometer using a high Faraday cup. During the course of the study, three international reference materials (2 HD-B1 and 1 LP-6) and two airshots (small amounts of air for ^{40}Ar-^{36}Ar ratio measurement) were analysed. The results are summarized in Table 1. The error for Ar analyses was below 1.00% and the average ^{40}Ar-^{36}Ar value of the air-shots yielded 296.03 ± 0.20. The general error for Ar analyses is below 1% (2 σ) based on the long-term precision of Ar measurements of the international reference materials. The K-Ar ages were calculated using ^{40}K abundance and decay constants recommended by Steiger and Jäger (1977). The age uncertainties account for the errors during sample weighing, ^{38}Ar-^{36}Ar and ^{40}Ar-^{38}Ar measurements and K analysis.

3.5. Synchrotron X-ray fluorescence microscopy (SXFM)

The XFM beamline at the Australian Synchrotron (Howard et al., 2020) was used to image thin sections of 30 μm thickness mounted on quartz slides and data were analysed as discussed in Akker (2020). Samples were scanned at 2 mm s^{-1} horizontally through an 18.5 keV X-ray beam focused to ~2 μm diameter by a Kirkpatrick-Baez mirror pair. A sampling interval in both the horizontal and vertical direction of 2 μm combined with the spot size yield a spatial resolution of ~2 μm with an effective per-pixel dwell of 1 ms. A Maia (Rev D) detector system positioned in its typical backscatter geometry was used to collect the excited fluorescence photons. All spectra were subsequently analysed using the Dynamic Analysis (Ryan and Jamieson, 1993) method as part of GeoPIXE (Ryan et al., 2005) and quantified using standard metallic foils, producing quantitative images of elements from sulphur to strontium. Due to the beamline and detection parameters, elements lighter than sulphur cannot be accurately quantified.

4. Results and interpretations

4.1. Mineralogy and mass proportion calculations

The whole-rock mineralogy of the slates consists of detrital clasts of calcite, quartz, dolomite and albite as well as primary chlorite and white mica. Accessory minerals are rutile and pyrite. White mica is the only K-bearing phase in this assemblage. There are no major differences in the mineral assemblage between the different samples, and in all samples, white mica occurs as dioctahedral potassic white mica of the 2M polytype, as confirmed by the absence of the 2.58 Å peak in the obtained diffractometer diagrams, which is consistent with the data of Hunziker et al. (1986). However, the sample with the lowest peak metamorphic temperature (sample A, 200 °C) shows the presence of minor swellable layers (Appendix Fig. B.1), which are most likely illite/smectite mixed layer minerals. The XRD spectra show that most of these mixed layer clays occur in the smallest grain size fraction (<0.8 μm) (Appendix Figure B.1). In all other samples, with peak metamorphic temperatures above 230 °C, such mixed-layers are absent, and this mineral group is dominated by a 2M polytype white mica (Appendix Figure B.2).

Mass proportion calculation indicates that the two coarse grain size fractions (4-32 μm and 32-64 μm) generally make up > 45% of the whole rock (Figs. 3 and 4). Sample E (300 °C) shows the smallest amount of phyllosilicates in almost each grain size fraction compared to all other samples (Fig. 4a). The amount of quartz and calcite versus phyllosilicates (white mica plus chlorite) increases with increasing grain size (orange shades against green shades in Fig. 4a). The largest amount of phyllosilicates, relative to quartz and calcite, is present in the smallest grain size fractions. Combining the results of the mass proportion calculations with the XRD data allows to obtain the absolute phase mass within each grain size fraction (Fig. 4b). This indicates that the grain size fraction <0.8 μm almost entirely consists of white mica. Chlorite was identified only in coarser grain size fractions >0.8 μm.

4.2. Microstructure – general cleavage formation

In the field, bedding and main cleavage orientation are mostly sub-parallel to each other. In some cases a macroscopic second oblique

Table 1
K-Ar on white mica data, reference materials and airshot data. K-Ar reference materials: HD-B1 (Hess and Lippolt, 1994), LP6 (Odin, 1982).

Sample ID	K	Rad. ^{40}Ar	Rad. ^{40}Ar	Rad.^{40}Ar/^{40}K	Age	Error
[μm]	[%]	[mol/g]	[%]	ratio	[Ma]	[Ma]
A <0.8	4.28	7.2412E-10	92.5	5.6683E-03	95.0	2.2
A 0.8-2	2.82	5.8755E-10	91.9	6.9804E-03	116.3	2.7
A 4-32	1.40	3.5406E-10	91.5	8.4730E-03	140.2	3.3
A whole rock	1.60	3.4116E-10	90.5	7.1437E-03	118.9	2.8
C <0.8	6.93	4.3943E-10	92.6	2.1244E-03	36.2	0.8
C 0.8-2	5.82	5.0204E-10	93.9	2.8900E-03	49.1	1.1
C 4-32	2.99	6.8714E-10	96.7	7.6995E-03	127.9	3.0
C whole rock	2.82	5.0474E-10	94.4	5.9966E-03	100.4	2.3
E <0.8	5.21	4.1726E-10	91.3	2.6832E-03	45.6	1.1
E 0.8-2.0	4.91	5.2446E-10	92.5	3.5786E-03	60.6	1.4
E 4-32	2.57	4.2886E-10	91.2	5.5907E-03	93.7	2.2
F <0.8	6.34	3.4190E-10	87.8	1.8067E-03	30.8	0.7
F 0.8-2	5.27	3.4714E-10	90.6	2.2069E-03	37.6	0.9
F 4-32	0.90	1.4348E-10	93.1	5.3650E-03	90.0	2.1
F whole rock	1.11	1.2264E-10	82.4	3.7017E-03	62.6	1.5
H 0.8-2.0	5.91	2.8027E-10	90.2	1.5888E-03	27.1	0.6
H 2-4	5.38	2.7499E-10	90.4	1.7125E-03	29.2	0.7
H 4-32	2.44	1.8919E-10	86.9	2.5977E-03	44.2	1.0
Standard ID	K	Rad. ^{40}Ar	Rad. ^{40}Ar	Age	Error	Error
	[%]	[mol/g]	[%]	[Ma]	[Ma]	to reference [%]
HD-B1-146	7.96	3.3542E-10	90.9	24.1	0.3	−0.29
HD-B1-149	7.96	3.3562E-10	90.9	24.2	0.3	−0.21
LP6-163	8.37	1.9234E-09	97.2	127.9	1.6	−0.04
Airshot ID	^{40}Ar/^{36}Ar	+/-				
AS140-AirS-1	295.25	0.23				
AS143-AirS-2	296.81	0.17				

cleavage exists. In thin section (e.g. sample F and H in Fig. 5), the alignment and interconnectivity of phyllosilicates together with the elongation of calcite and quartz grains along the metamorphic and strain gradient forms an increasingly anisotropic planar fabric. In the SXFM element maps, chlorite is indicated by elevated Fe concentrations, and white mica is identified by elevated Rb concentrations (Fig. 5). The low-temperature and low-strain sample (Fig. 5a) shows chlorite, white mica and fossils (mainly Globigerina) in a fine-grained matrix. The alignment of phyllosilicates forms a weak fabric. With increasing temperature, pressure and background deformation, the fabric becomes stronger, and at 320 °C and intermediate-strain a wavy cleavage exists (Fig. 5b). The high-temperature and high-strain end member at 330 °C shows a regular and narrowly spaced cleavage (Fig. 5c). Here, the cleavage comprises mostly white mica. Chlorite mainly precipitates in the pressure shadows of the fossils (Fig. 5c and Fig. 6b,c). The latter is indicative for pressure-dissolution and precipitation, which is the dominant ductile deformation mechanism in these rocks (Akker, 2020). Note that individual segments of Globigerina chambers show clear evidence for partial dissolution while retaining their initial round shape even up to the highest strain and temperature (Fig. 5). Therefore, any shape change of these strong clasts is accommodated by pressure dissolution (Fig. 5c).

4.3. Phyllosilicate morphology and chemistry

Comparing two carbonate-rich slates with increasing temperatures (Fig. 6a-b, i.e. 200 °C and 320 °C) indicates that (i) phyllosilicates increase in grain size due to grain growth and (ii) both white mica and chlorite start to interconnect, evolving into phyllosilicate-rich cleavage planes (Fig. 6b). In this way the main layer-parallel cleavage becomes interconnected by an oblique one. These phyllosilicate-rich cleavage planes separate quartz and calcite grains. The initial absence of the oblique cleavage planes (Fig. 6a) suggests recrystallization of newly formed grains with increasing metamorphic grade. Shearing-induced passive rotation of existing grains could have already resulted in the formation of the main layer-parallel cleavage domain. However, the SEM data provide evidence for neocrystallization by precipitation of phyllosilicates in pore space and grain boundaries (Fig. 6d,e,f).

With increasing metamorphic grade and strain, the quartz and calcite grains become elongated, indicating that the grain edges dissolve. The dissolution of detrital quartz and calcite accommodates flattening perpendicular to the main compression direction. Simultaneous stretching parallel to the extension directions provides space for precipitation. Precipitation comprises the cleavage-parallel oriented growth of quartz and calcite with elongated shape and precipitation of phyllosilicates on the cleavage planes in the same orientation as the elongated grains (compare Fig. 6a-b). On the grain scale, three types of phyllosilicate grains have been identified (Fig. 7c, grains i-iii): i) mixed aggregates of white mica and chlorite, often deformed, bent or with an oblique angle to the main cleavage, ii) large elongated grains (~ 50 μm long) of white mica or chlorite, aligned parallel to the S0 or S1 and, iii) small grains (~ 10 μm long) of white mica or chlorite, either parallel or oblique to the S0 or S1, or overgrowing other phases such as quartz and calcite.

In the low-temperature sample (230 °C; Fig. 7a), the white mica composition shows an exchange between Na and K (Fig. 7d, paragonite exchange; Parra et al. (2002)). Towards higher temperatures (330 °C), this trend changes to white mica compositions showing an alkali deficiency, which is caused by the pyrophyllite substitution ($(Na, K)^{xii}Al^{iv} = \square^{xii}Si^{iv}$), where □ = vacancy (Fig. 7d-e) (Parra et al., 2002). The large white mica grain in sample H (Fig. 7c, spot 1 and 2) still shows the detrital composition, whereas the small grains (Fig. 7, spot 4) already show the new recrystallized composition including a pyrophyllite

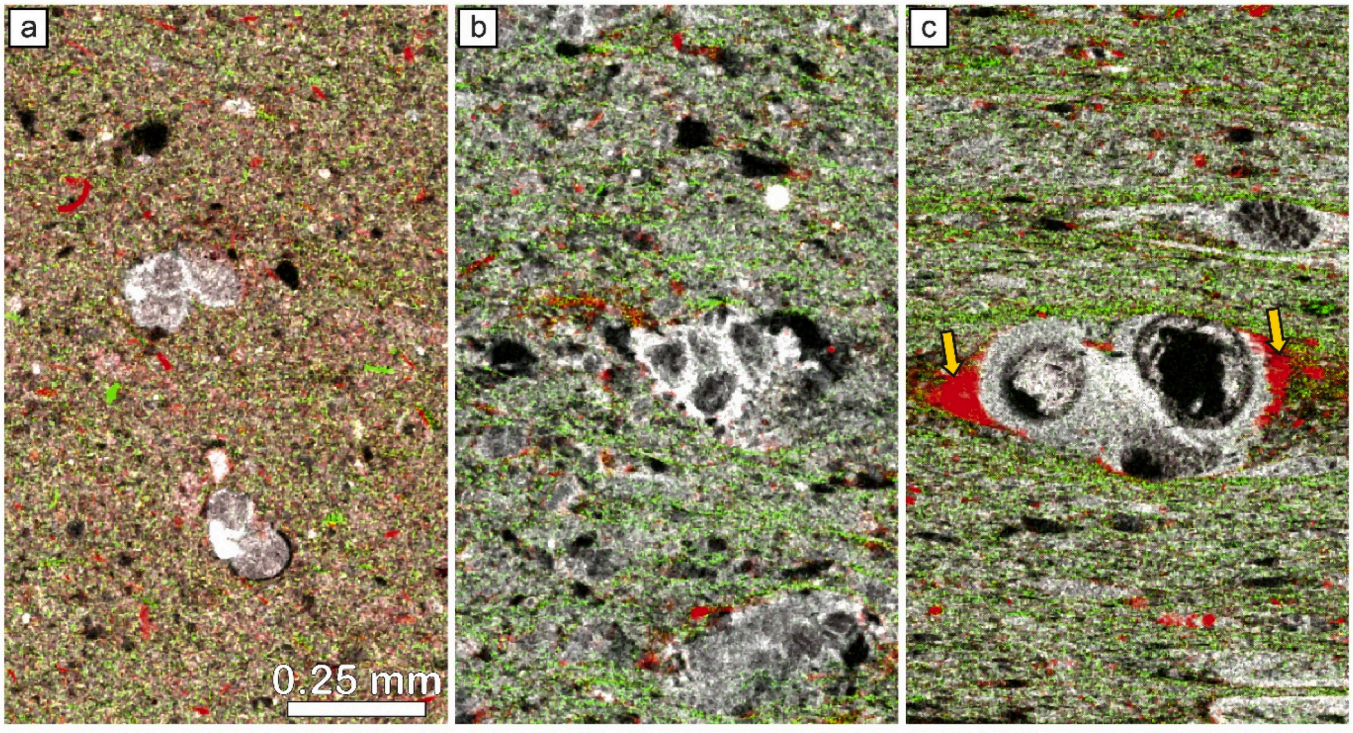

Fig. 5. SXFM maps of microstructures (Sr in greyscale, Fe in red, Rb in green). a) The low-temperature and low-strain endmember (sample A, 200 °C) shows only a weak fabric defined by the weak alignment of phyllosilicates. This can be best seen by weakly oriented chlorite platelets (high Fe concentrations, red). b) The intermediate-temperature and intermediate-strain sample (sample F, 320 °C) shows a moderate fabric, made up by a wavy spaced cleavage, best seen by alignment of phyllosilicates (green Rb layers). c) The high-temperature and high-strain endmember (sample H, 330 °C) shows a strong planar fabric, with regular and narrow spaced cleavage domains (alignment of phyllosilicates as seen by green Rb layers). Chlorite precipitates in the pressure shadows of fossils (high Fe concentrations in red: yellow arrows).(For interpretation of the references to color in this figure legend, the reader is referred to the web version of this article.)

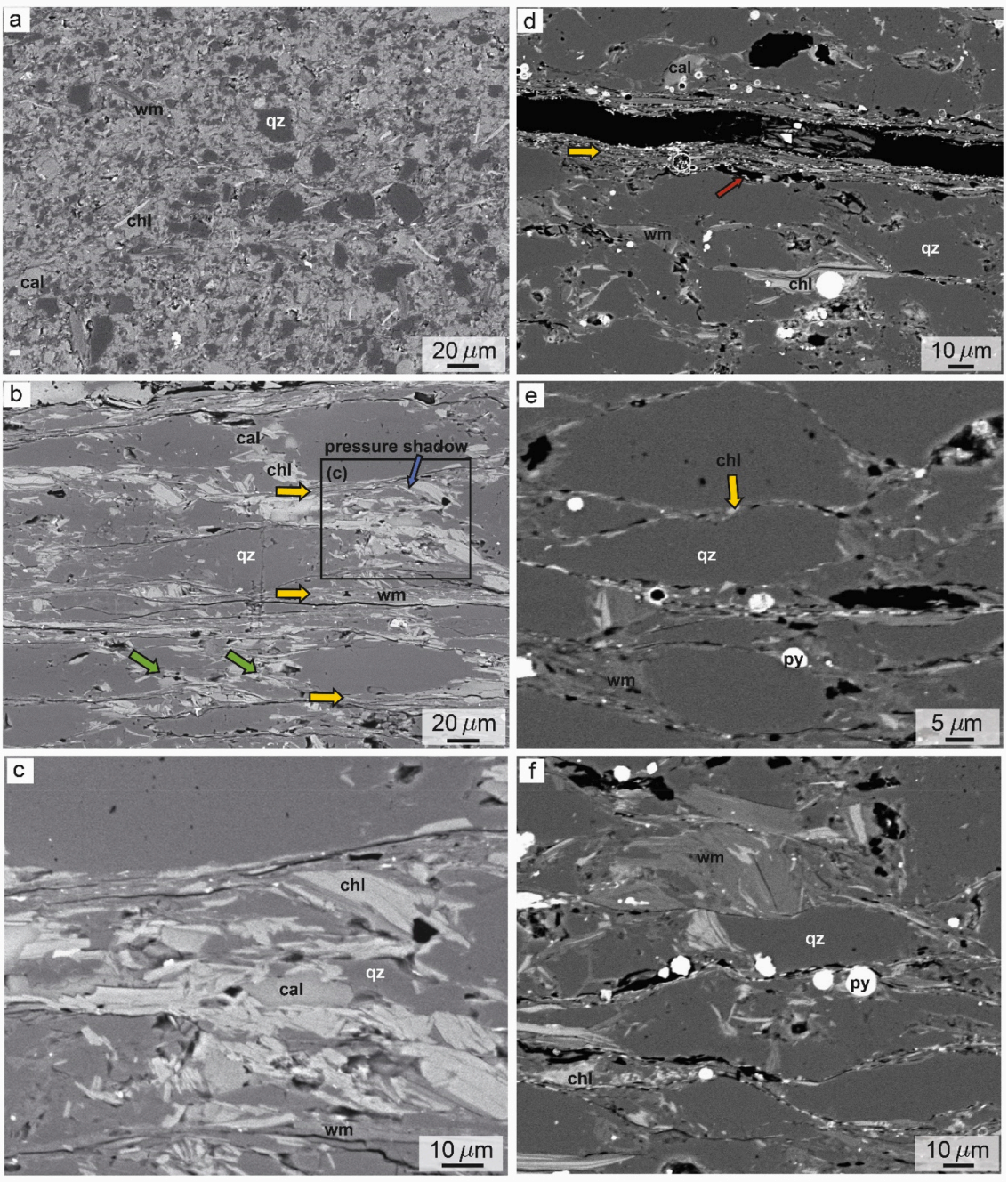

Fig. 6. Microstructures observed in BSE images. a) Low-temperature endmember (sample A, 200 °C) of carbonate-rich slate shows phyllosilicate grains in fine-grained matrix. b) High-temperature sample (sample G, 320 °C) of quartz-rich slate shows strong alignment and interconnectivity of phyllosilicates forming main layer-parallel cleavage (yellow arrows) and oblique cleavage planes (green arrows). Chlorite grains are significantly larger than in low-temperature endmember (a) and precipitate predominantly in pressure shadows, which are filled by a polyphase mixture of: chlorite (chl), white mica (wm), calcite (cal) and quartz (qz) (see zoom in (c). d) Quartz-rich slate shows layers of aligned fine-grained phyllosilicates (yellow arrow). New phyllosilicates (small grains) precipitate in pore space (red arrow) and on grain boundaries, starting to form connected layers (e). f) Besides, small phyllosilicate grains precipitating on grain boundaries, large phyllosilicates (tens of microns) are present in the matrix. Images from (d), (e) and (f) are same sample with sample coordinates: 46°57′36.4”N 9°11′23.6”E.(For interpretation of the references to color in this figure legend, the reader is referred to the web version of this article.)

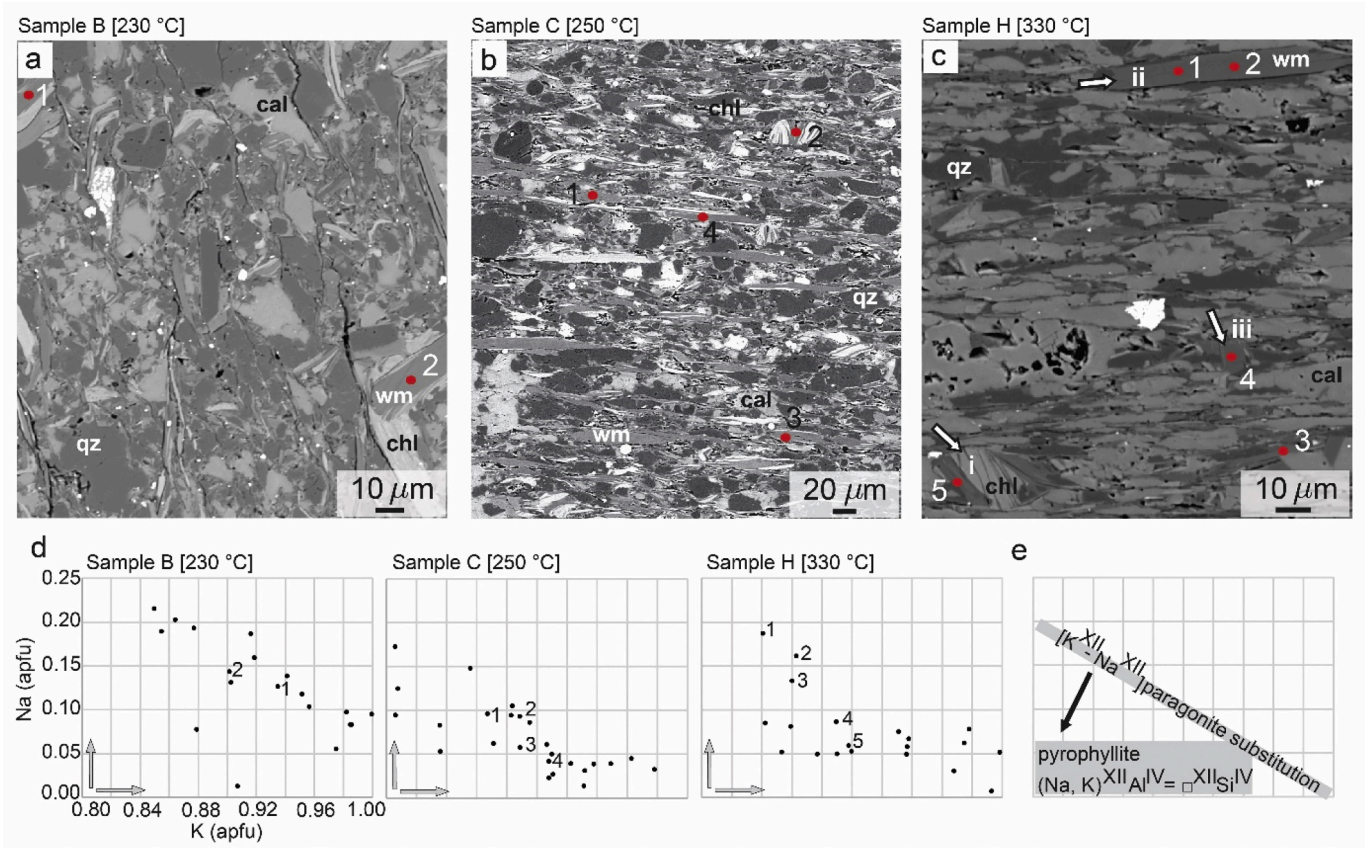

Fig. 7. BSE images of microstructures (a-c) and microprobe chemistry of white mica (d-e) along metamorphic gradient. a-c) Microstructural changes along metamorphic gradient. The high temperature sample H (330 °C) shows three different phyllosilicate morphologies (i,ii,iii): see text for explanation. d) Na vs. K plots of white mica (x-axis and y-axis same for all plots; apfu: atoms per formula unit) along the increasing temperature gradient show an enhanced pyrophyllite exchange in white mica. Note that variations in the paragonite substitution within detrital grains (spot 1 and 2 in (c)) could be the effect of zonations. e) Schematic overview of main trend (black arrow) along metamorphic gradient in (d) which changes from the paragonite to the pyrophyllite exchange in white mica.

substitution component. However, not all grains follow this trend, for example the relatively small grain in Fig. 7c (spot 3), which still shows the detrital composition, or a composition in between the two end members.

4.4. K-Ar data of white mica

The apparent K-Ar age data as well as reference materials and airshot data are given in Table 1. As white mica is the only K-bearing phase in these rocks, the results can be used as proxy for chemical processes in white mica. Illite/smectite mixed-layer minerals, such as those seen in sample A (Appendix Fig. B.1), as well as mixed aggregates of white mica and chlorite cannot be physically separated and are therefore present within the measured fractions. Two trends are observed in the K-Ar data (Fig. 8a): (i) all apparent ages increase with increasing grain size and (ii) apparent ages decrease with increasing metamorphic grade. This implies that the amount of white mica recrystallization increases with increasing metamorphic grade. In order to quantify the amount of white mica recrystallization along the metamorphic gradient, we use a diagram of grain size versus isotopic ratio (Fig. 8b). Besides plotting the measured isotopic ratios for sample C, this diagram also displays two potential end members. The first one is the end member approximating the purely detrital composition, representing the starting material which is derived from coarse-grained granites from the hinterland (Lihou and Allen, 1996; Sinclair, 1997). This yields the respective rad. ^{40}Ar-^{40}K ratio in the primary detrital grains calculated from the age of 280 Ma (see the age equation in Appendix C and Table C.1). For detrital mica from these granites, we infer a typical coarse grain size of about 500 μm. The lower fine-grained end member represents a completely recrystallized sample and is calculated with the minimum assumption of about 20 Ma (Hunziker et al., 1986; Nibourel, 2019; Nibourel et al., 2018). For this sample, we infer a fine grain size of about 0.1 μm, which is the limit of the theoretical expected smallest grain size and commonly used in literature (e.g. (Torgersen et al., 2015b); Zwingmann et al., 2004). By plotting these two end members in the diagram of Fig. 8b and calculating a linear regression it is possible to estimate the amount of recrystallization for any specific grain size in between the two end members. This approach is only feasible by neglecting rad. ^{40}Ar loss by diffusion (see overview in Section 5.3). These estimates of recrystallization of each grain size are combined with the amount of micas in each grain size fraction obtained by quantitative XRD. In this way, the ratio between detrital and newly formed micas (recrystallized proportion) in each grain size fraction is estimated (Fig. 8c). The results indicate that (i) the absolute portion of detrital grains increases with increasing grain size and (ii) with increasing metamorphic grade, the amount of recrystallization increases (Fig. 8d).

5. Discussion

In the following sections, we discuss the relationship between Ar data, mineral chemistry and microstructure and present an interpretation of the K-Ar data in the context of the geological setting and aim to gain better insight in the quantification of the resetting processes.

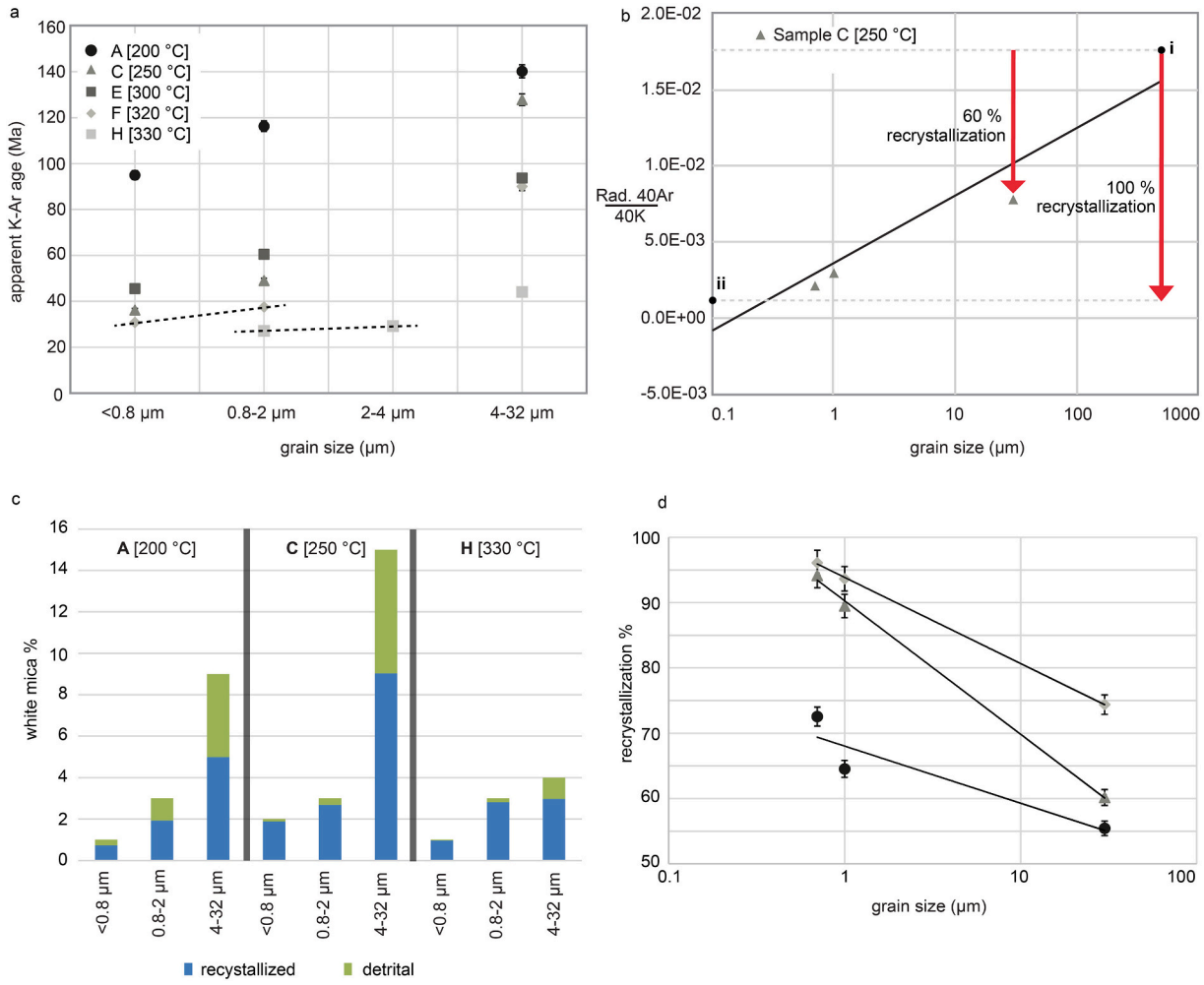

Fig. 8. K-Ar age data combined with mineralogy indicates amount of recrystallization. a) Plot of grain size over apparent K-Ar age shows that K-Ar apparent ages increase with increasing grain size for all samples. With increasing metamorphic grade apparent ages decrease. Once they approach a stable value, the age can be interpreted as real (dashed black lines). If error bars are not shown they fall within the data markers. b) Recrystallization curve with two end members: (i) detrital end member (0% recrystallization) and (ii) recrystallized end member (100% recrystallization). c) Mineralogical quantification of XRD data combined with recrystallization curve in (b) indicates the absolute percentage of white mica per grain size fraction. With increasing grain size the relative amount of recrystallized white mica grains decreases. d) Plot of grain size over percentage of recrystallization shows that the amount of recrystallized white mica grains increases with metamorphic grade and decreases with grain size. In some cases error bars are not visible at scale.

5.1. *The relation between Ar data, mineral chemistry and microstructure*

Excluding Ar diffusion as resetting process, most analysed grain size fractions of white mica reflect a mixture of non- or partially reset grains (detrital grains) with newly formed grains (recrystallized). With increasing metamorphic gradient, the amount of recrystallized white mica increases (Fig. 8). Along this trend the mineral chemistry of white mica changes from a composition dominated by the paragonite component to a composition dominated by the pyrophyllite component.

Assuming that the proportion of detrital grains decreases with increasing metamorphic grade, we link the detrital chemistry to the paragonite component. However, not all large grains, which are often assumed to be detrital, preserve the detrital chemistry; some show a chemistry closer to the recrystallized chemistry, indicating partial resetting of detrital grains. Similarly, not all small grains are recrystallized. Some small grains preserve the detrital composition and thus must have survived to higher metamorphic temperatures. This indicates that newly formed grains form in a large range of grain size fractions in the investigated samples, which could be the effect of grain coarsening with increasing metamorphic grade or of the different processes of the formation of new grains (Berger et al., 2017). However, the isotopic variation, showing decreasing apparent ages with increasing metamorphic grade (Fig. 8a), is directly connected to the microstructure. As the result of pressure solution, new fine grains precipitate on cleavage planes and in pressure shadows, the proportion of both increases along the metamorphic gradient (Figs. 5 and 6). The phyllosilicate-rich cleavage layers involve small grains, with grain sizes up to 10 µm. The development of such layers requires new recrystallization and reorganization of the rocks structure. Therefore, measuring radiogenic ^{40}Ar in one grain size fraction from this evolving microstructure, which is a function of deformation mechanism and finite strain (Airaghi et al., 2018; Cossette et al., 2015; Mulch et al., 2005), yields different amounts of radiogenic ^{40}Ar along the metamorphic and strain gradient. The complete understanding of the development of cleavage formation is missing, but new grains precipitate by dissolution-precipitation processes and affect the measured radiogenic ^{40}Ar resulting in increasingly younger apparent ages with increasing metamorphic grade.

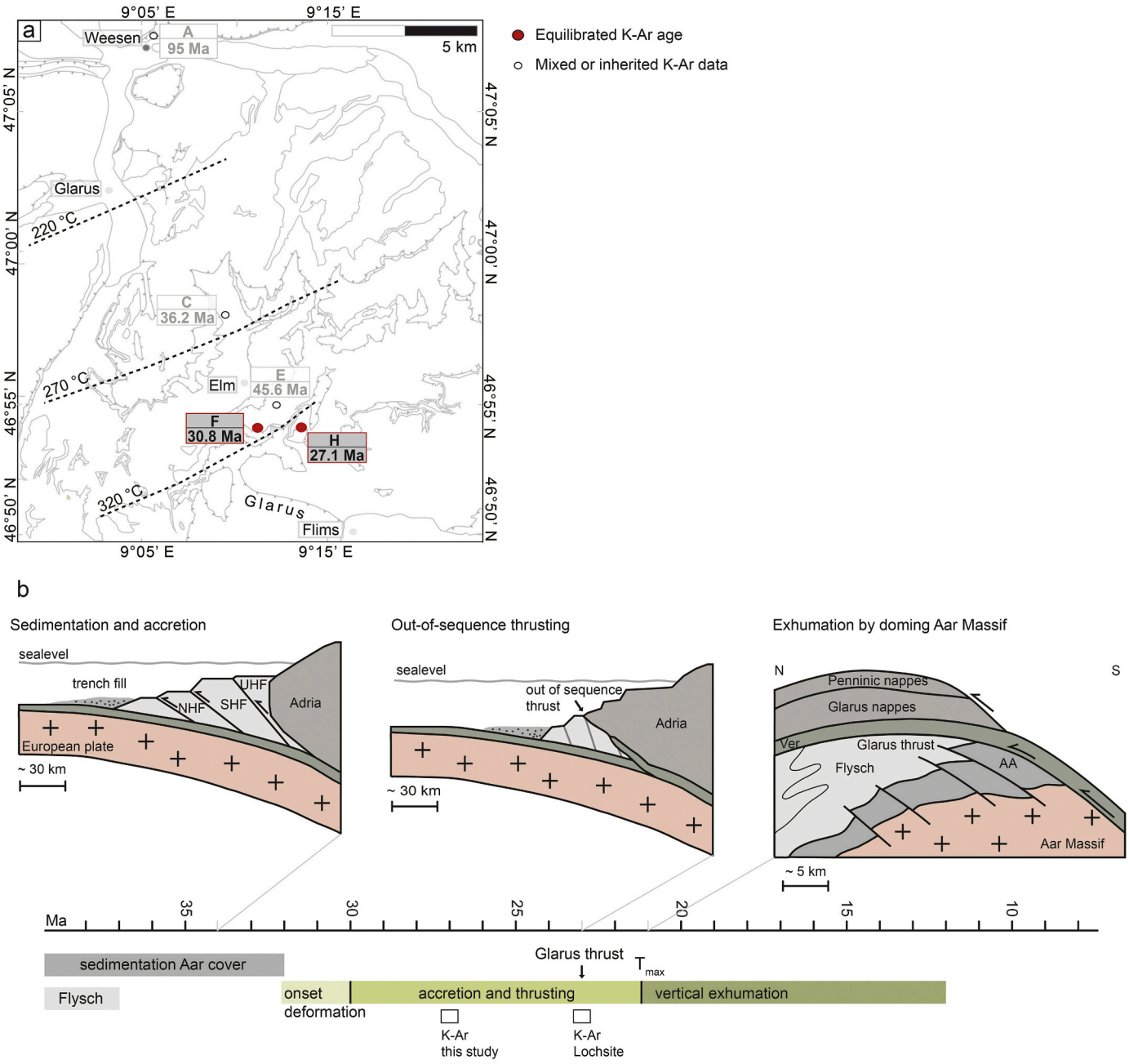

Fig. 9. Geological interpretation of obtained K-Ar ages in this study. a) Geological map as presented in Fig. 1 with plotted isograds after a compilation of temperature data from Ebert et al. (2007), Rahn et al. (1995) and Lahfid et al. (2010). The age data of the smallest grain size fractions are plotted and only sample F and H at the highest metamorphic temperature yield an age which is close to the real age. b) Sedimentation and accretion is followed by out-of-sequence thrusting and eventually exhumation by doming of the Aar Massif. K-Ar age Lochsite from Hunziker et al. (1986), Tmax of Aar Massif basement from Nibourel et al. (2018), right figure modified after Pfiffner (1993).

5.2. The meaning of the K-Ar data in a regional context

The highest amount of isotopic resetting is expected in the smallest grain size at the highest investigated metamorphic grade with highest deformation, as represented by sample H, 0.8-2 μm. This sample yields an apparent K-Ar age of 27.1±0.6 Ma (Table 1), indicating major deformation of the Flysch at ~27 Ma (Fig. 9a). The Flysch units are deformed continuously in the accretionary wedge before onset of the main out-of-sequence Glarus thrust (Dielforder et al., 2016). The main microstructures described in this study are related close to T_{max} conditions. The main Helvetic thrusting, including the Glarus thrust, has to be younger than the youngest sediments on top of the Aar Massif at 34-32 Ma (Fig. 9b) (Fischer and Villa, 1990; Lu et al., 2019). The Glarus thrust and the investigated underlying Flysch units experienced coeval deformation due to the exhumation of the underlying basement (Aar Massif; Herwegh et al. (2008)). The timing of T_{max} in the basement of the central Aar Massif is 22-20 Ma (Nibourel et al., 2018; Rolland et al., 2009), which is close to a zircon fission track age of about 19 Ma in the Vättis window (Michalski and Soom, 1990). The Vättis window is in near vicinity to the non-exhumed basement of the Glarus area. Therefore, from a regional point of view, the deformation of the Flysch units and the Glarus thrust had to be active between 32 Ma (youngest sediment) and ~20 Ma (T_{max} of the exhumed basement). The mineral fractions of sample F (<0.8 μm) and sample H (0.8-2 and 2-4 μm) in this study fall in this time interval. Moreover, the data of sample H flatten out in a grain size versus apparent age diagram (Fig. 8a). The only direct isotope data out of the Glarus thrust indicates ages between 25-20 Ma (Hunziker et al., 1986), which is close to our obtained 27 Ma age considering the tectonic evolution summarized in Fig. 9.

5.3. Isotopic resetting: Ar diffusion and recrystallization

The meaning of white mica ages with regard to Ar diffusion is widely discussed in the literature (e.g. Allaz et al. (2011); Dodson (1973); Harrison et al. (2009); Kirschner et al. (1996); Villa (2016); Villa and Hanchar (2017)). However, recrystallization and a series of replacement structures are also known to affect the mineral chemistry and isotope data (e.g. Airaghi et al. (2017); Berger et al. (2017); Villa and Hanchar (2017)). In the sections above, microstructural and chemical evidence demonstrate the presence of recrystallization of white micas at all

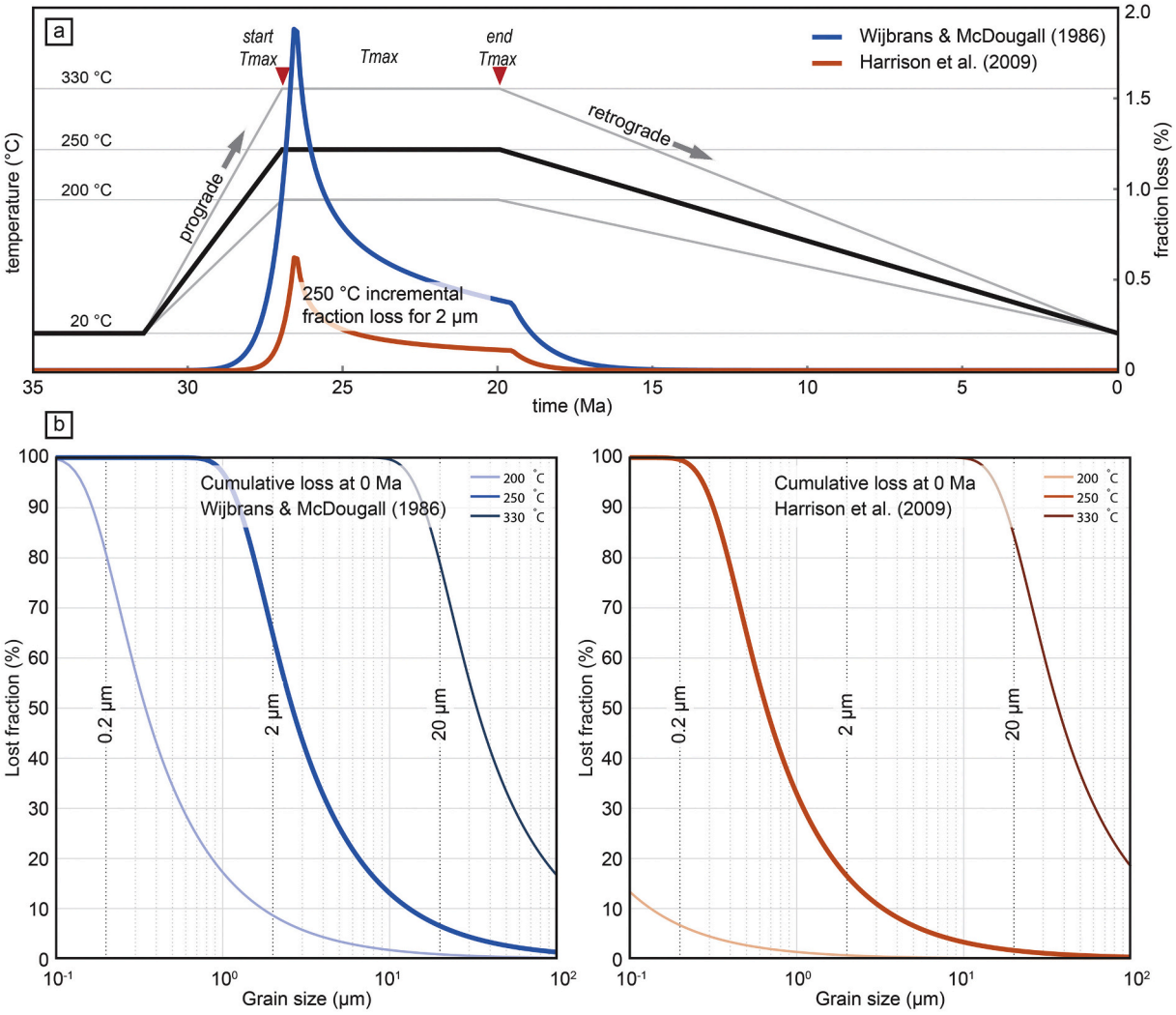

Fig. 10. Diffusion modelling results. a) Temperature-time path (prograde, Tmax and retrograde) with varying Tmax used for Ar diffusion modelling. Blue and red curve indicate incremental Ar fraction loss for the two different diffusion coefficients. Incremental loss is shown for 2 μm grain size and peak metamorphic temperature of 250 °C. Note that depending on temperature and grain size the shape of the curves slightly deviate from the presented ones. However, the shown model is a good indicator for when fraction loss occurs along the T-t path. b) Cumulative loss for discussed grain sizes and diffusion coefficients (resp. blue, red) at 0 Ma (present day).

temperature conditions and for all grain sizes. Moreover, an increasing degree of recrystallization is observed with increasing temperature (Fig. 8). Hence, the question arises: what is the influence of recrystallization versus diffusion on the final Ar budget? Three hypotheses can be postulated. The measured variations in rad. $^{40}Ar/^{40}K$ ratios might be (a) purely volume diffusion-controlled, (b) purely recrystallization-controlled or (c) controlled by a combination of both, potentially with variable contribution of each process with increasing temperature. The hypothesis (c) implies potential loss or Ar from detrital grains as well as from newly formed grains by volume diffusion at or near Tmax. To test these hypotheses, we estimate the effect of diffusion with simple diffusion models at the temperatures and grain sizes of interest. For this purpose, we use the analytical solution of Watson et al. (2010) for an infinite slab to model Ar diffusion (Appendix D). This choice corresponds to the assumption that micas are thin platelets, which lose their Ar by outgassing along the shortest spatial axis (perpendicular to cleavage) (Figure D.1). Watson et al. (2010) show that the infinite-slab model produces appropriate results for this geometry if the ratio of diffusivities along the crystallographic axes is < 10. The model calculates retained Ar fraction (G) for 0.1 Ma increments in the temperature-time space. The main controlling parameters are the evolution of both temperature and the related diffusion coefficient with time and the grain size (Fig. 10; Appendix D). The change in temperature with time is defined by the geological history of the investigated samples (see above and Fig. 9; Ebert et al. (2007); Hunziker et al. (1986); Lahfid et al. (2010); Nibourel et al. (2018); Pfiffner (1993); Rahn et al. (1995)). The prograde path starts with the termination of sedimentation of the Tavayannaz sandstone at 32 Ma (the youngest sediment of the investigated Flysch sequence) and the initial temperature is defined at 20°C (Fig. 10). The prograde path ends at peak metamorphic conditions (Tmax) at ~27 Ma. Peak metamorphic temperature in the studied Flysch units was reached by the overthrusting of the Upper Helvetic nappe stack, namely during activity of the Glarus thrust (Ebert et al., 2007; Herwegh et al., 2008; Lahfid et al., 2010). Peak metamorphism lasted until 20 Ma, the latter correlating to the timing of the onset of vertical exhumation of the basement (see above). For the peak metamorphic temperature, we use three scenarios (200°C, 250°C, and 330°C, see Fig. 10) representing T-t paths at three locations along the general N-S temperature gradient. On the retrograde path, the temperature decreases to 20°C at 0 Ma (Fig. 10). The diffusion calculations were carried out for different characteristic diffusion lengths, assuming that grain sizes are a direct measure for the diffusion length. Only limited diffusion coefficients have been experimentally determined for white mica phyllosilicates (Wijbrans and McDougall (1986) and Harrison et al. (2009)). We applied both diffusion coefficients in our modelling (Figure D.2 and Table D.1). The solution of Watson et al. (2010) results in a fraction loss (F = 1-G) of the diffusing species depending on the following factors: temperature, time, diffusion length (grain size), diffusion coefficient and the activation energy (Appendix D). An extract of these results is summarized in Table 2.

At low temperatures (200°C), values for Ar loss by diffusion calculated for the Wijbrans and McDougall (1986) diffusion coefficient are at peak metamorphic conditions in the range of <1 to 16%, with the exception of the very small fraction, which results in a fraction loss of 76%. For the Harrison et al. (2009) diffusion coefficient, fraction loss is in the range of <1 to 6% and can be neglected in terms of rejuvenation of ages for all grain size fractions. With these values and given that the detrital input is Permian in age, we would expect to obtain Permian/Triassic K-Ar ages and a grain-size-age relation for samples that underwent a low Tmax path (~200 °C). However, the resulting apparent ages of our samples are Upper Cretaceous (Table 1). This clearly demonstrates that the measured Ar values in such samples are controlled by other processes than Ar volume diffusion, which could be recrystallization.

At temperatures of about 250°, the used diffusion coefficients would indicate potential Ar loss for the grain size fraction of 0.2 and 2 μm at peak metamorphic temperatures. For grain sizes > 10 μm Ar loss is still

Table 2
Fraction loss in % at start and end of Tmax and at 0 Ma calculated for three Tmax scenarios (200°C, 250°C and 330°C) and three grain sizes (0.2 μm, 2 μm, 20 μm) with input parameters from Wijbrans and McDougall (1986) and Harrison et al. (2009).

	200°C			250°C			330°C		
	fraction loss at start Tmax	fraction loss at end Tmax	fraction loss at 0 Ma	fraction loss at start Tmax	fraction loss at end Tmax	fraction loss at 0 Ma	fraction loss at start Tmax	fraction loss at end Tmax	fraction loss at 0 Ma
Wijbrans and McDougall (1986)									
0.2 μm	16.10%	76.20%	80.80%	94.90%	100.00%	100.00%	100.00%	100.00%	100.00%
2 μm	1.61%	7.96%	8.63%	12.00%	60.10%	64.60%	99.00%	100.00%	100.00%
20 μm	0.16%	0.80%	0.86%	1.20%	6.05%	6.54%	15.10%	74.50%	78.95%
Harrison et al., 2009									
0.2 μm	1.04%	6.31%	6.67%	25.10%	99.30%	99.60%	100.00%	100.00%	100.00%
2 μm	0.10%	0.63%	0.67%	2.51%	15.60%	16.50%	98.10%	100.00%	100.00%
20 μm	0.01%	0.06%	0.07%	0.25%	1.56%	1.65%	14.00%	81.60%	84.45%

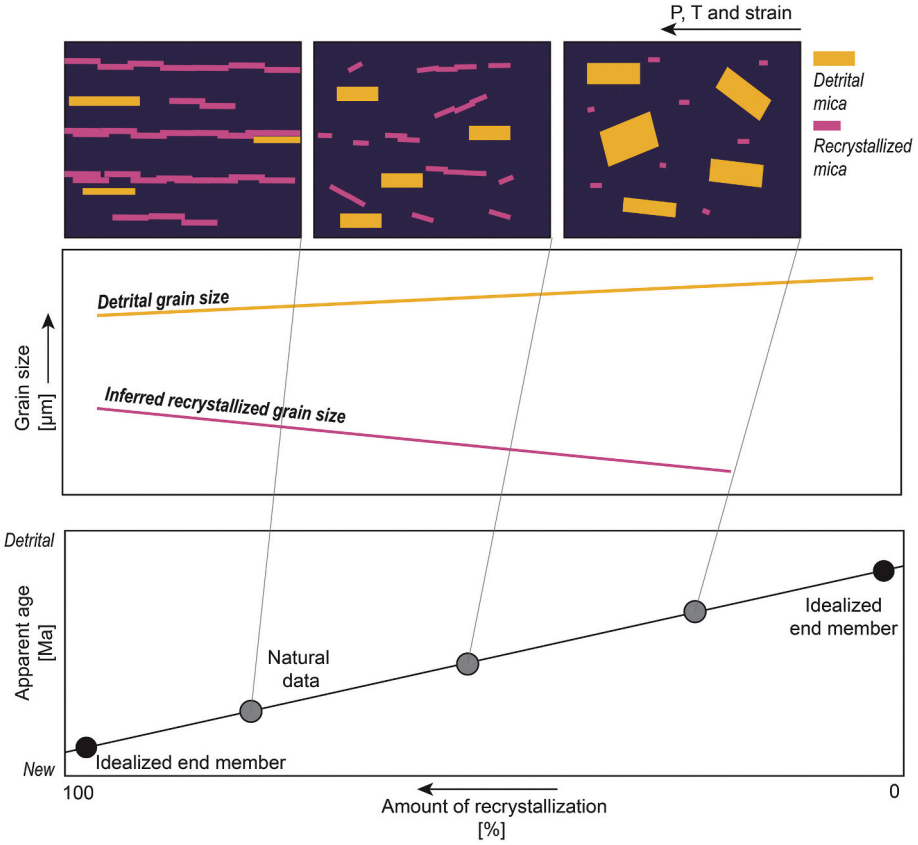

Fig. 11. Schematic figure showing the relation between microstructure, grain sizes and apparent K-Ar age as a function of the amount of recrystallization.

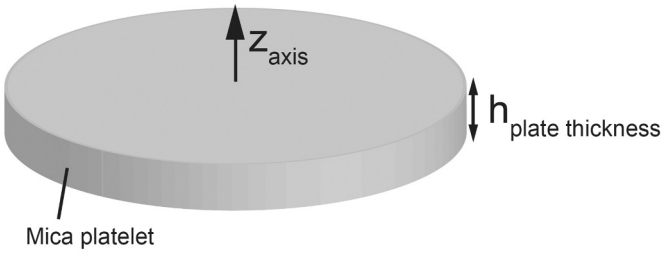

Fig. D.1. Schematic flat cylinder with anisotropy ratio for diffusivity <10, which justifies the use of the infinite slab model after Watson et al. (2010).

minor, which means a loss less than <15% (Wijbrans and McDougall, 1986) and <5% (Harrison et al., 2009) of Ar in the detrital grains along the prograde path and at peak metamorphic conditions. However, the small grains show significant loss (up to 100%) of Ar at peak metamorphism conditions for both diffusion coefficients (relevant for age determination of new grains, see for example calculations of Huon et al. (1994); Kirschner et al. (1996)). For large grain sizes (>10 µm), diffusion alone cannot explain the measured isotopic ratios, which still yield Cretaceous ages. However, small grain sizes, which are more affected by Ar loss due to thermal diffusion, are still not entirely reset by recrystallization, as is seen by their apparent age. It is therefore likely that a combination of volume diffusion and recrystallization processes play a role at intermediate temperatures (~250°C).

At high temperatures (~330°C), the large grains still retain a substantial amount of Ar at the beginning of peak metamorphic temperatures, yielding ages which show an inherited Ar component from detrital grains. Smaller grains (<10 µm) lose about all their Ar and show the expected age of the main deformation phase in this area. This indicates that the system is chemically reset, which either could be entirely due to volume diffusion itself, or by completed recrystallization (Fig. 8).

Our microstructural and mineral-chemical data (Figs. 5, 6, 7) demonstrate the occurrence of recrystallization as the result of dissolution-precipitation processes, which increases along the metamorphic and background strain gradient. The associated phyllosilicate cleavage planes show a grain-size reduction of detrital grains and grain growth of recrystallized grains along the studied gradient (Fig. 11). Numerous studies in literature have reported that recrystallization or replacement structures can change chemistry and rad. ^{40}Ar-content of the micas (e.g. Airaghi et al. (2017); Berger et al. (2017)). Owing to aforementioned inconsistencies between models and measurements, such recrystallization processes outside pure volume diffusion are most likely in charge to rejuvenate the apparent mica ages at low temperatures (Fig. 11). We also show that recrystallization/resetting is more pronounced and complete with increasing metamorphic temperatures. However, at high temperatures (~330°C) it remains difficult to resolve the contribution of the two end member processes, volume diffusion and recrystallization. Given the fact that recrystallization is becoming

pervasive, classical volume diffusion is of minor relevance. However, it becomes a major Ar resetting process for completely recrystallized samples that sit for long times at peak metamorphic temperatures > 300°C.

6. Conclusion

The changing isotope and mineral chemistry data of white mica in slates during increasing metamorphism is related to a microstructural development of spaced cleavage formed by the precipitation of phyllosilicates controlled by dissolution-precipitation creep. The data indicate that chemical resetting of the isotopic K-Ar system is controlled by this ductile deformation mechanism. Increasing strain requires larger amounts of mass transfer, which directly affects the isotopic resetting of the minerals. The relationship between isotopic resetting and grain size is not simple as seen by the chemical changes in white mica along the studied temperature gradient. However, most of the small grains (< 10 μm) include newly formed, recrystallized or chemically reset grains. These recrystallized grains precipitate out of solution and form the spaced cleavage of the slates, whereas the large grains, (partly) preserve the detrital composition. Therefore, apparent ages in such slates depend on the selected grain size as well as the amount and type of deformation, of which the intensity changes with metamorphic grade. The combination of quantification of a certain grain size fraction, mineral quantities and the K-Ar system represents therefore a valuable tool to estimate the amount of recrystallization in white mica in slates. Hence, this tool can be of great interest when estimating the amount of dehydration and fluid liberation in fossil accretionary wedges. Knowledge of time-integrated liberation of fluids is fundamental in understanding the mechanics of accretionary wedges, where the amount of available fluid controls fast seismic versus slow aseismic deformation. Only in the case of a nearly complete resetting, reliable age information of deformation can be gained by the presented approach, else quantitative information on the amount of recrystallization of the phyllosilicate spectrum can be obtained. With respect to a regional geological perspective, therefore only the smallest white mica fractions with the highest volume of reset material result in a geological meaningful age of 27.1±0.6 Ma, which is in close agreement with the timing of the dominating deformation phase in this area of the European Alps.

Author contributions

MH and AB designed the project. Together with IVA, MH and AB collected the samples and IVA carried out the microstructural characterisation, SEM work, geochemical analyses and grain size separations. HZ and AT performed the K-Ar measurements on the grain size separates. IVA together with CES, MWMJ and CMK carried out the SXFM measurements. CES and TCS carried out volume diffusion calculations. IVA analysed all data and prepared the manuscript with contributions from all authors.

Funding

This work was supported by the Swiss National Science Foundation (SNSF, grant number 162340).

Declaration of Competing Interest

The authors declare that they have no known competing financial interests or personal relationships that could have appeared to influence the work reported in this paper.

Acknowledgements

We thank Martin Fisch for his contributions to the X-ray diffraction (XRD) analysis and Pierre Lanari for assistance with the microprobe. Synchrotron X-ray fluorescence microscopy (SXFM) was undertaken on the X-ray Fluorescence Microscopy (XFM) beamline at the Australian Synchrotron, part of ANSTO.

Appendix A. Sample information

Table A.1
Sample overview. Peak metamorphic temperatures from Ebert et al. (2007), Rahn et al. (1995) and Lahfid et al. (2010).

Sample ID	Sample name	Latitude	Longitude	Lithology	Peak temperature (°C)
A	16W01	47°08'26.3″ N	9°06'26.1″ E	slate	200
B	16SCH01B	46°59'47.2″ N	9°05'20.9″ E	slate	230
C	17LP06	46°58'12.0″ N	9°09'19.7″ E	slate	250
D	16KR4	46°57'34.3″ N	9°11'23.6″ E	slate	270
E	17N1B	46°54'17.5″ N	9°12'11.3″ E	calcareous slate –vein array	300
F	16MM01	46°53'29.0″ N	9°11'22.4″ E	calcareous slate	320
G	16SP01	46°54′07.4″ N	9°13′28.6″ E	slate	320
H	16SS01	46°53'02.8″ N	9°13'28.8″ E	slate	330

Appendix B. XRD quantification

For quantitative phase analyses of XRD data the following crystal structures are used from the Inorganic Crystal Structure Database (ICSD): quartz (No: 67121), calcite (No: 73446), albite (No: 68913), dolomite (No: 100680), muscovite (No: 180081), chamosite (No: 80080), chlorite (No: 164234), illite (No: 90144), siderite (No: 100678), pyrite (No: 15012), rutile (No: 36412), corundum (No: 51687). For dolomite, calcite, albite and the Rietveld clay-phases, preferred orientation corrections were applied. For the clay minerals Rietveld refinements, octahedral Al/Fe occupancies were refined in the case of muscovite/illite, and octahedral Mg/Fe occupancies were refined in chamosite/chlorite.

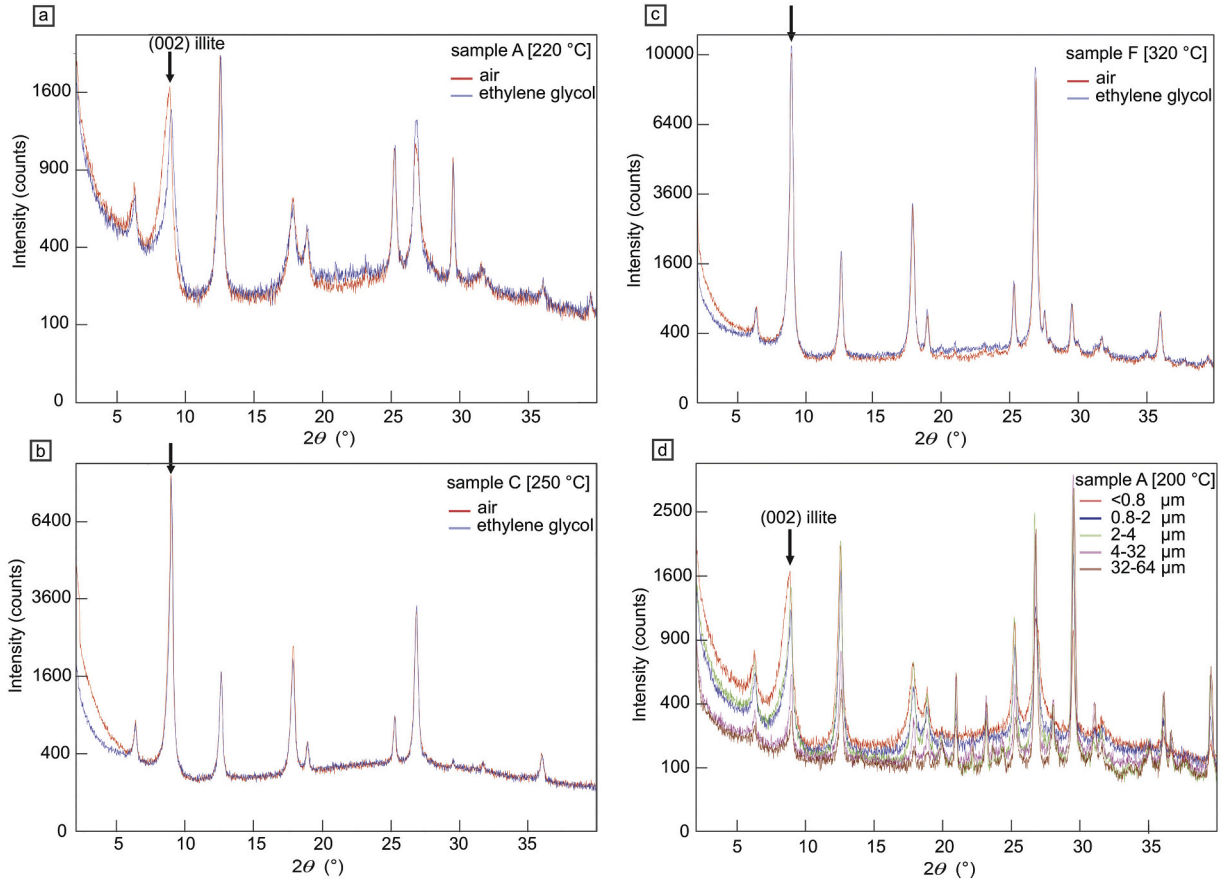

Fig. B.1. XRD spectra from oriented samples on glass plates. a) Low temperature sample A shows a strong shift in the illite peak measured in air and after 24 h in ethylene glycol environment, indicating the presence of swellable clay minerals. b) Intermediate temperature sample C shows no shift in the illite peak between in air and after ethylene glycol treatment, indicating the absence of swellable clays. c) High temperature sample F shows no shift in the illite peak between in air and after ethylene glycol treatment, indicating the absence of swellable clay minerals. d) The grain size fractions of sample A measured in air show an increase in asymmetry of the illite peak with decreasing grain size, indicative for the presence of mixed interlayers.

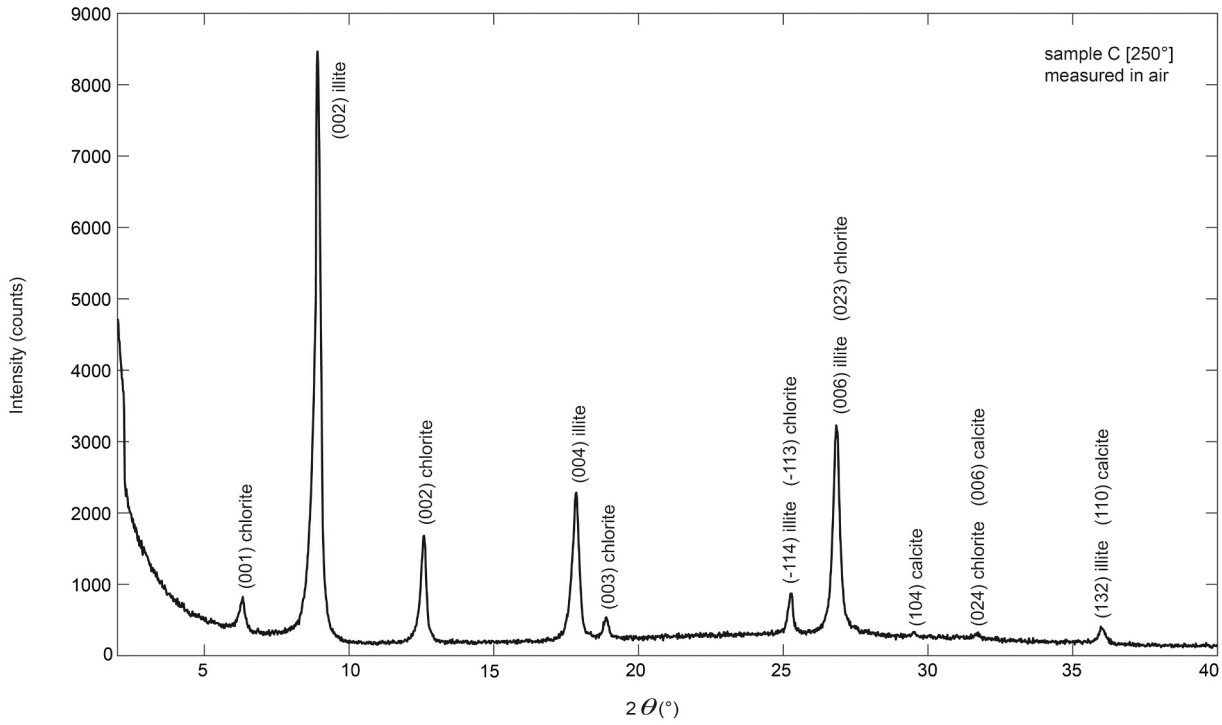

Fig. B.2. XRD spectra with indicated Miller indices from oriented sample C on glass plates measured in air. Within this spectra polymorphs 1M and 2M of illite are indistinguishable.

Appendix C. Age equation

The K-Ar age equation reads (Faure, 1977):

$$40Ar^{*} = \frac{\lambda e}{\lambda} 40K(e^{\lambda t} - 1) \quad \text{(C.1)}$$

Where:
$40Ar^{*}$= accumulated radiogenic $40Ar$
λe= decay of $40K$ to $40Ar$ (0.581 x 10^{-10} y^{-1})
λ = total decay constant of $40K$ (5.543 x 10^{-10} y^{-1})
$40K$ = measured concentration of $40K$
t = age of the mineral (y)
This equation can be solved for the *40Ar*/40K* ratio:

$$\frac{40Ar^{*}}{40K} = \frac{(e^{\lambda t} - 1)\lambda e}{\lambda} \quad \text{(C.2)}$$

Table C.1
Input parameters and values for end member calculations plotted in Fig. 8b.

Endmember	Age (Ma)	Inferred grain size (μm)	40Ar*/40K
100% detrital (i)	280	500	$1.76E^{-2}$
100% recrystallized (ii)	20	0.1	$1.17E^{-3}$

Appendix D. Diffusion modelling

There are known difficulties in calculating the reference diffusion coefficient D_0, because of existing problems with experimental data (Hess et al., 1987; Villa, 2010; Villa et al., 2014). Regardless of these uncertainties, we use the reference diffusion coefficient determined by Wijbrans and McDougall (1986) and Harrison et al. (2009) (see table D.1) due to the sparse existence of more accurate data.

Table D.1
Input parameters from Wijbrans and McDougall (1986) and Harrison et al. (2009).

	D_0 (m^2/s)	Ea (J/mol)	K_b (J/molK)
Wijbrans and McDougall (1986)	6.03×10^{-11}	1.67×10^{5}	8.31
Harrison et al., 2009	1.99×10^{-2}	2.64×10^{5}	8.31

Eq. (D.1) Arrhenius-type relation for the temperature dependence of diffusivity:

$$D = D_0 e^{-Ea/(K_b T)} \quad \text{(D.1)}$$

D = diffusion coefficient in m^2/s
D_0 = reference diffusion coefficient in m^2/s
Ea = activation energy in J mol^{-1}
K_b = Boltzman constant in J mol^{-1} K^{-1}
T = temperature in K
Eq. (D.2) for fraction G of diffusant retained in an infinite slab (from Watson et al. (2010))

$$G = \frac{1}{h}\int_{-\frac{h}{2}}^{\frac{h}{2}} dz Z(z,t) = \frac{8}{\pi^2}\sum_{n}^{\infty} \frac{1}{(2n+1)^2}\pi^2 y(t) \quad \text{(D.2)}$$

$$y(t) = \int_0^t \frac{D(t')}{h^2} dt \quad \text{(D.3)}$$

With h denotes, the slab thickness, $y(t)$ the dimensionless release coordinate Eq. (D.3) and D the diffusivity along the z axis. Note that the solution for the retained fraction G, y and D are identical to G_3, y_3 and D_{33}, respectively in Watson et al. (2010), Eq. 10 & Eq. 32. Based on the fraction of retained diffusant, the loss fraction F is obtained as:

$$F = 1 - G \quad \text{(D.4)}$$

The following (Appendix D, Fig. D.2) are results for one T-t path (Tmax is 250°C) and two different diffusion coefficients (Harrison et al., 2009; Wijbrans and McDougall, 1986). We select this example, because at lower Tmax (200°C) loss fraction of Ar by diffusion is very small and can be neglected. On the contrary, at higher metamorphic temperature (Tmax: 330°C) the loss fraction of Ar by diffusion yields mostly values around 100% (see Table 2 and explanation in the text).

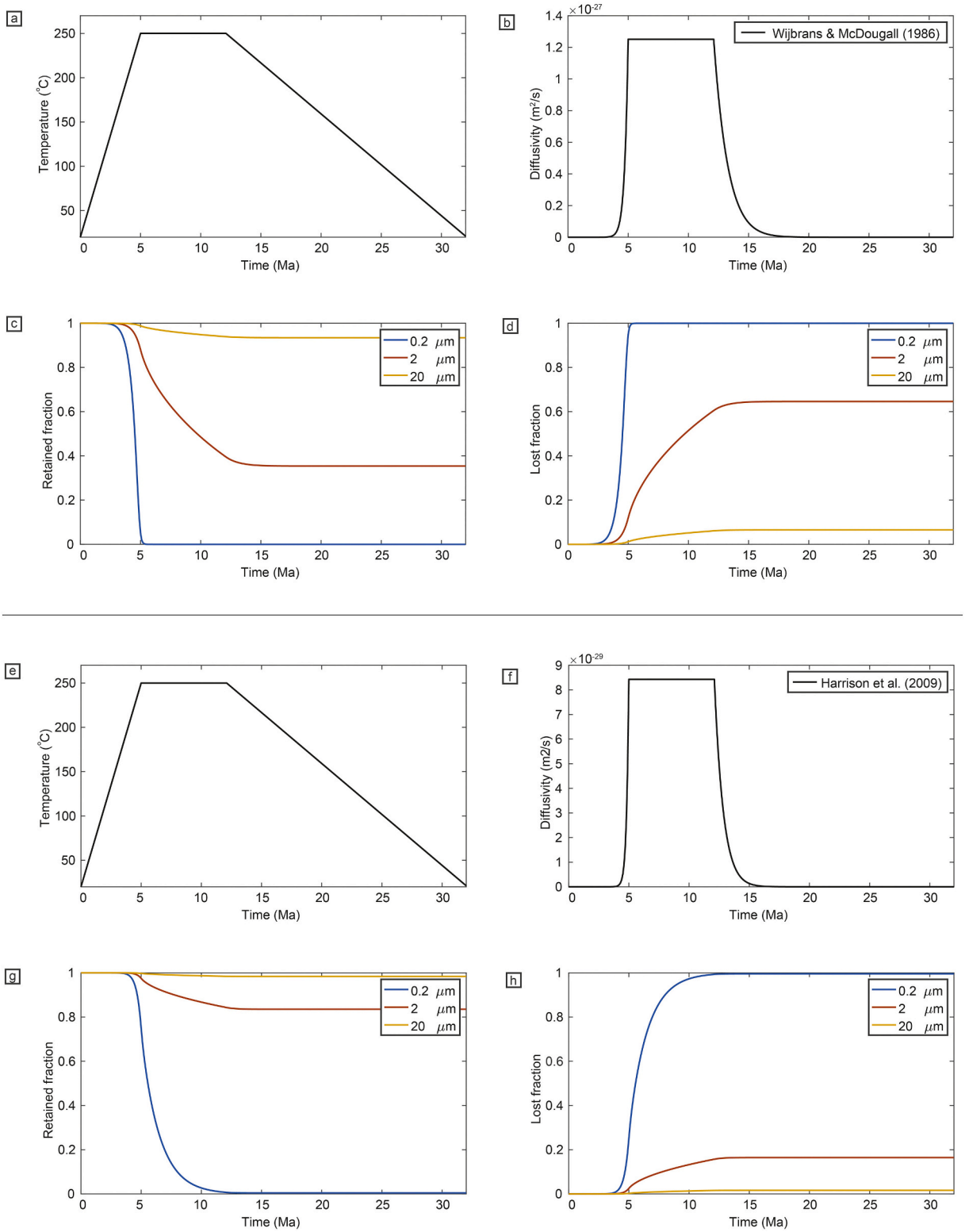

Fig. D.2. Diffusion modelling along the entire temperature-time path for Tmax is 250°C calculated with input parameters from Wijbrans and McDougall (1986) (a-d) and Harrison et al. (2009) (e-h). a) Temperature-time path for Tmax is 250°C. Note that the time axis is starting at 0 Ma, which corresponds to the start of the burial at 32 Ma. b) Diffusivity calculated along the temperature-time path. c) Retained fraction of Ar and d) Lost fraction of Ar. Note, this is the inverse of (c). e-h) Same plots as (a) to (d) but with input parameters from Harrison et al. (2009).

Appendix E. Supplementary data

Supplementary data to this article can be found online at https://doi.org/10.1016/j.tecto.2020.228708.

References

Airaghi, L., Lanari, P., de Sigoyer, J., Guillot, S., 2017. Microstructural vs compositional preservation and pseudomorphic replacement of muscovite in deformed metapelites from the Longmen Shan (Sichuan, China). Lithos 282, 262–280.

Airaghi, L., Warren, C.J., de Sigoyer, J., Lanari, P., Magnin, V., 2018. Influence of dissolution/reprecipitation reactions on metamorphic greenschist to amphibolite facies mica 40Ar/39Ar ages in the Longmen Shan (eastern Tibet). J. Metamorph. Geol. 36, 933–958.

Akker, I.V., 2020. The Evolution of Slate Microstructures during the Accretion of Foreland Basin Sediments and Implications for Mechanical Strength, Fluid Flow and Seismicity in Accretionary Wedges (Unpublished) (Dissertation). Institute of Geological Sciences, Faculty of Science.

Allaz, J., Engi, M., Berger, A., Villa, I.M., 2011. The effects of retrograde reactions and of diffusion on 40Ar–39Ar ages of micas. J. Petrol. 52, 691–716.

Berger, A., Wehrens, P., Lanari, P., Zwingmann, H., Herwegh, M., 2017. Microstructures, mineral chemistry and geochronology of white micas along a retrograde evolution: An example from the Aar massif (Central Alps, Switzerland). Tectonophysics 721, 179–195.

Bonhomme, M., 1975. Methode de datation potassium-argon: appareillage et technique. Université Louis Pasteur, Strasbourg, France, p. 53.

Bosse, V., Villa, I.M., 2019. Petrochronology and hygrochronology of tectono-metamorphic events. Gondwana Res. 71, 76–90.

Clauer, N., 2013. The K-Ar and 40Ar/39Ar methods revisited for dating fine-grained K-bearing clay minerals. Chem. Geol. 354, 163–185.

Clauer, N., Środoń, J., Francu, J., Šucha, V., 1997. K-Ar dating of illite fundamental particles separated from illite-smectite. Clay Miner. 32, 181–196.

Clauer, N., Zwingmann, H., Liewig, N., Wendling, R., 2012. Comparative 40Ar/39Ar and K–Ar dating of illite-type clay minerals: A tentative explanation for age identities and differences. Earth Sci. Rev. 115, 76–96.

Cossette, É., Schneider, D., Warren, C., Grasemann, B., 2015. Lithological, rheological, and fluid infiltration control on 40Ar/39Ar ages in polydeformed rocks from the West Cycladic detachment system, Greece. Lithosphere 7, 189–205.

Dempster, T., 1992. Zoning and recrystallization of phengitic micas: implications for metamorphic equilibration. Contrib. Mineral. Petrol. 109, 526–537.

Dielforder, A., Vollstaedt, H., Vennemann, T., Berger, A., Herwegh, M., 2015. Linking megathrust earthquakes to brittle deformation in a fossil accretionary complex. Nat. Commun. 6.

Dielforder, A., Berger, A., Herwegh, M., 2016. The accretion of foreland basin sediments during early stages of continental collision in the European Alps and similarities to accretionary wedge tectonics. Tectonics 35 (10), 2216–2238.

Dodson, M.H., 1973. Closure temperature in cooling geochronological and petrological systems. Contrib. Mineral. Petrol. 40, 259–274.

Dunlap, W.J., Teyssier, C., McDougall, I., Baldwin, S., 1991. Ages of deformation from K/Ar and 40Ar/39Ar dating of white micas. Geology 19, 1213–1216.

Ebert, A., Herwegh, M., Pfiffner, A., 2007. Cooling induced strain localization in carbonate mylonites within a large-scale shear zone (Glarus thrust, Switzerland). J. Struct. Geol. 29, 1164–1184.

Faure, G., 1977. Principles of Isotope Geology.

Fischer, H., Villa, I., 1990. Erste K/Ar-und 40Ar/39Ar-Hornblende-Mineralalter des Taveyannaz-Sandsteins. Schweiz. Mineral. Petrogr. Mitt. 70, 73–75.

Fitz-Diaz, E., van der Pluijm, B., 2013. Fold dating: A new Ar/Ar illite dating application to constrain the age of deformation in shallow crustal rocks. J. Struct. Geol. 54, 174–179.

Harrison, T.M., Célérier, J., Aikman, A.B., Hermann, J., Heizler, M.T., 2009. Diffusion of 40Ar in muscovite. Geochim. Cosmochim. Acta 73, 1039–1051.

Heinrichs, H., Herrmann, A.G., 2013. Praktikum der analytischen Geochemie. Springer-Verlag.

Herwegh, M., Hürzeler, J.-P., Pfiffner, O.A., Schmid, S.M., Abart, R., Ebert, A., 2008. the Glarus thrust: excursion guide and report of a field trip of the swiss tectonic studies Group (swiss Geological society, 14.–16. 09. 2006). Swiss J. Geosci. 101, 323–340.

Hess, J., Lippolt, H., 1994. Compilation of K/Ar measurements on HD-B1 standard biotite; 1994 status report, Phanerozoic time scale. In: Bull. Liasis. Inform. IUGS Subcom. Geochronol, pp. 19–23.

Hess, J., Lippolt, H., Wirth, R., 1987. Interpretation of 40Ar39Ar biotites: Evidence from hydrothermal degassing experiments and TEM studies. Chem. Geol.: Isotope Geosci. Sect. 66, 137–149.

Howard, D.L., de Jonge, M.D., Afshar, N., Ryan, C.G., Kirkham, R., Reinhardt, J., Kewish, C.M., McKinlay, J., Walsh, A., Divitcos, J., 2020. The XFM beamline at the Australian Synchrotron. J. Synchrotron Radiat. 27, 1447–1458.

Hunziker, J., Frey, M., Clauer, N., Dallmeyer, R., Friedrichsen, H., Flehmig, W., Hochstrasser, K., Roggwiler, P.T., Schwander, H., 1986. The evolution of illite to muscovite: mineralogical and isotopic data from the Glarus Alps, Switzerland. Contrib. Mineral. Petrol. 92, 157–180.

Huon, S., Burkhard, M., Hunziker, J.-C., 1994. Mineralogical, K-Ar, stable and Sr isotope systematics of K-white micas during very low-grade metamorphism of limestones (Helvetic nappes, western Switzerland). Chem. Geol. 113, 347–376.

Kemp, S.J., Gillespie, M.R., Leslie, G.A., Zwingmann, H., Campbell, S.D.G., 2019. Clay mineral dating of displacement on the Sronlairig Fault: implications for Mesozoic and Cenozoic tectonic evolution in northern Scotland. Clay Miner. 54, 181–196.

Kirschner, D.L., Cosca, M.A., Masson, H., Hunziker, J.C., 1996. Staircase 40/Ar39Ar spectra of fine-grained white mica: Timing and duration of deformation and empirical constraints on argon diffusion. Geology 24, 747–750.

Lahfid, A., Beyssac, O., Deville, E., Negro, F., Chopin, C., Goffé, B., 2010. Evolution of the Raman spectrum of carbonaceous material in low-grade metasediments of the Glarus Alps (Switzerland). Terra Nova 22, 354–360.

Lemoine, M., Trümpy, R., 1987. Pre-oceanic rifting in the Alps. Tectonophysics 133, 305–320.

Lihou, J.C., Allen, P.A., 1996. Importance of inherited rift margin structures in the early North Alpine Foreland Basin, Switzerland. Basin Res. 8, 425–442.

Lu, G., Di Capua, A., Winkler, W., Rahn, M., Guillong, M., von Quadt, A., Willett, S.D., 2019. Restoring the source-to-sink relationships in the Paleogene foreland basins in the Central and Southern Alps (Switzerland, Italy, France): a detrital zircon study approach. Int. J. Earth Sci. 108, 1817–1834.

McDonald, C.S., Warren, C.J., Mark, D.F., Halton, A.M., Kelley, S.P., Sherlock, S.C., 2016. Argon redistribution during a metamorphic cycle: consequences for determining cooling rates. Chem. Geol. 443, 182–197.

Michalski, I., Soom, M., 1990. The Alpine thermo-tectonic evolution of the Aar and Gotthard massifs, central Switzerland: fission track ages on zircon and apatite and K-Ar mica ages. Schweiz. Mineral. Petrogr. Mitt. 70, 373–387.

Moore, J.C., Saffer, D., 2001. Updip limit of the seismogenic zone beneath the accretionary prism of southwest Japan: an effect of diagenetic to low-grade metamorphic processes and increasing effective stress. Geology 29, 183–186.

Mulch, A., Cosca, M.A., 2004. Recrystallization or cooling ages: in situ UV-laser 40Ar/39Ar geochronology of muscovite in mylonitic rocks. J. Geol. Soc. 161, 573–582.

Mulch, A., Cosca, M., Andresen, A., Fiebig, J., 2005. Time scales of deformation and exhumation in extensional detachment systems determined by high-spatial resolution in situ UV-laser 40Ar/39Ar dating. Earth Planet. Sci. Lett. 233, 375–390.

Nibourel, L., 2019. The Structural and Thermo-kinetic Evolution of the Eastern Aar Massif. Philosophisch-naturwissenschaftliche Fakultät Universität Bern, Switzerland.

Nibourel, L., Berger, A., Egli, D., Luensdorf, N.K., Herwegh, M., 2018. Large vertical displacements of a crystalline massif recorded by Raman thermometry. Geology 46, 879–882.

Odin, G., 1982. Interlaboratory Standards for Dating Purposes.

Parra, T., Vidal, O., Agard, P., 2002. A thermodynamic model for Fe–Mg dioctahedral K white micas using data from phase-equilibrium experiments and natural pelitic assemblages. Contrib. Mineral. Petrol. 143, 706–732.

Passchier, C.W., Trouw, R.A., 2005. Microtectonics. Springer Science & Business Media.

Pawley, G., 1981. Unit-cell refinement from powder diffraction scans. J. Appl. Crystallogr. 14, 357–361.

Pevear, D.R., 1999. Illite and hydrocarbon exploration. Proc. Natl. Acad. Sci. 96, 3440–3446.

Pfiffner, O.A., 1993. The structure of the Helvetic nappes and its relation to the mechanical stratigraphy. J. Struct. Geol. 15, 511–521.

Pfiffner, O.A., Ramsay, J., Schmid, S., 2011. Structural map of the Helvetic Zone of the Swiss Alps. Geol. Specl. Map 1.

Putnis, A., 2002. Mineral replacement reactions: from macroscopic observations to microscopic mechanisms. Mineral. Mag. 66, 689–708.

Rahn, M., Mullis, J., Erdelbrock, K., Frey, M., 1995. Alpine metamorphism in the north Helvetic flysch of the Glarus-Alps, Switzerland. Eclogae Geol. Helv. 88, 157–178.

Rolland, Y., Cox, S.F., Corsini, M., 2009. Constraining deformation stages in brittle–ductile shear zones from combined field mapping and 40Ar/39Ar dating: the structural evolution of the Grimsel Pass area (Aar Massif, Swiss Alps). J. Struct. Geol. 31, 1377–1394.

Rüefli, W.H., 1959. Stratigraphie und Tektonik des eingeschlossenen Glarner Flysches im Weisstannental (St. Galler Oberland). ETH Zurich.

Ryan, C.G., Jamieson, D.N., 1993. Dynamic analysis: on-line quantitative PIXE microanalysis and its use in overlap-resolved elemental mapping. Nucl. Inst. Methods Phys. Res. B 77, 203–214.

Ryan, C.G., Etschmann, B.E., Vogt, S., Maser, J., Harland, C.L., van Achterbergh, E., Legnini, D., 2005. Nuclear microprobe - synchrotron synergy: Towards integrated quantitative real-time elemental imaging using PIXE and SXRF. Nucl. Inst. Methods Phys. Res. B 231, 183–188.

Schmid, S.M., 1975. The Glarus Overthrust: Field Evidence and Mechanical Model.

Sinclair, H., 1997. Tectonostratigraphic model for underfilled peripheral foreland basins: an Alpine perspective. Geol. Soc. Am. Bull. 109, 324–346.

Steiger, R.H., Jäger, E., 1977. Subcommission on geochronology: convention on the use of decay constants in geo-and cosmochronology. Earth Planet. Sci. Lett. 36, 359–362.

Torgersen, E., Viola, G., 2014. Structural and temporal evolution of a reactivated brittle–ductile fault–Part I: fault architecture, strain localization mechanisms and deformation history. Earth Planet. Sci. Lett. 407, 205–220.

Torgersen, E., Viola, G., Zwingmann, H., Harris, C., 2015a. Structural and temporal evolution of a reactivated brittle–ductile fault–Part II: timing of fault initiation and reactivation by K–Ar dating of synkinematic illite/muscovite. Earth Planet. Sci. Lett. 410, 212–224.

Torgersen, E., Viola, G., Zwingmann, H., Henderson, I.H., 2015b. Inclined K–Ar illite age spectra in brittle fault gouges: effects of fault reactivation and wall-rock contamination. Terra Nova 27, 106–113.

van der Pluijm, B.A., Vrolijk, P.J., Pevear, D.R., Hall, C.M., Solum, J., 2006. Fault dating in the Canadian Rocky Mountains: Evidence for late Cretaceous and early Eocene orogenic pulses. Geology 34, 837–840.

Villa, I.M., 2010. Disequilibrium textures versus equilibrium modelling: geochronology at the crossroads. Geol. Soc. Lond. Spec. Publ. 332, 1–15.

Villa, I.M., 2016. Diffusion in mineral geochronometers: Present and absent. Chem. Geol. 420, 1–10.

Villa, I.M., Hanchar, J.M., 2013. K-feldspar hygrochronology. Geochim. Cosmochim. Acta 101, 24–33.

Villa, I.M., Hanchar, J.M., 2017. Age discordance and mineralogy. Am. Mineral. J. Earth Planet. Mater. 102, 2422–2439.

Villa, I.M., Bucher, S., Bousquet, R., Kleinhanns, I.C., Schmid, S.M., 2014. Dating polygenetic metamorphic assemblages along a transect across the Western Alps. J. Petrol. 55, 803–830.

Viola, G., Zwingmann, H., Mattila, J., Käpyaho, A., 2013. K-Ar illite age constraints on the Proterozoic formation and reactivation history of a brittle fault in Fennoscandia. Terra Nova 25, 236–244.
Wang, Y., Zwingmann, H., Zhou, L., Lo, C.-h., Viola, G., Hao, J., 2016. Direct dating of folding events by 40Ar/39Ar analysis of synkinematic muscovite from flexural-slip planes. J. Struct. Geol. 83, 46–59.
Watson, E.B., Wanser, K.H., Farley, K.A., 2010. Anisotropic diffusion in a finite cylinder, with geochemical applications. Geochim. Cosmochim. Acta 74, 614–633.
White, S., Knipe, R., 1978. Microstructure and cleavage development in selected slates. Contrib. Mineral. Petrol. 66, 165–174.
Wijbrans, J.R., McDougall, I., 1986. 40 Ar/39 Ar dating of white micas from an Alpine high-pressure metamorphic belt on Naxos (Greece): the resetting of the argon isotopic system. Contrib. Mineral. Petrol. 93, 187–194.
Zwingmann, H., Offler, R., Wilson, T., Cox, S., 2004. K–Ar dating of fault gouge in the northern Sydney Basin, NSW, Australia—Implications for the breakup of Gondwana. J. Struct. Geol. 26, 2285–2295.
Zwingmann, H., Berger, A., Eggenberger, U., Todd, A., Herwegh, M., 2017. Testing high-voltage electrical discharges in disintegrating claystone for isotopic and mineralogical studies: an example using Opalinus claystone. Clay Clay Miner. 65, 342–354.
Zwingmann, H., den Hartog, S.A., Todd, A., 2019. The effect of sub-seismic fault slip processes on the isotopic signature of clay minerals–Implications for K-Ar dating of fault zones. Chem. Geol. 514, 112–121.